NIXO-Based Identification of the Dominant Terms in a Nonlinear Equation of Motion of Structures with Geometric Nonlinearity

Michael Kwarta[1] and Matthew S. Allen[2]

[1] University of Wisconsin - Madison, Mechanical Engineering Department
1500 Engineering Drive, Engineering Research Building, Madison, WI 53706, USA
Email address: kwarta@wisc.edu

[2] Brigham Young University, Mechanical Engineering Department
350B Engineering Building, Provo, UT 84602, USA
Email address: matt.allen@byu.edu

Abstract

The objective of this publication is to propose a novel technique for black-box identification of structures with geometric nonlinearity. The technique is based on a recently introduced frequency-domain system identification method called Nonlinear Identification through eXtended Outputs (NIXO). The proposed algorithm first expresses the nonlinear part of modal equation of motion (EOM) as a general polynomial of high order, and then removes the terms which are determined to be irrelevant to the mechanical system's response. This division into dominant and irrelevant nonlinear terms relies on the values of two novel indicators that are particular to NIXO. The heuristic presented here was observed to work well only when the tested structure is excited with various swept-sine input signals of different magnitudes (so that the system oscillates at sufficiently distinctive amplitudes in different experimental tests). The technique is first demonstrated on a noise-free numerical case study employing a reduced model of a curved beam. The results obtained are verified via comparing the true Nonlinear Normal Mode (NNM) to the one computed using the modal EOM pointed out by NIXO. Then the method is demonstrated on experimental measurements collected on a 3D-printed flat beam exhibiting significant natural frequency shifts, and the outcomes are verified by overlaying the identified NNMs on the swept-sine responses.

Keywords: Black-Box Nonlinear System Identification, NIXO, Nonlinear Experimental Dynamics, Geometrically Nonlinear Structures, Swept-Sine Vibration Testing

1 Introduction

Nonlinear oscillating systems are receiving a lot of attention in both industry and academia due to current as well as potential future industrial applications. In many fields, nonlinearities are recognized as important in obtaining accurate predictive models of structures such as aircraft, spacecraft and automotive systems. For example, nonlinear structural dynamics helps in modeling frictional mechanical systems [1,2], or predicting the motion of structures oscillating at high-amplitudes [3–5]. Vibration mitigation has lately become a popular field of study employing the nonlinear approach [6–8]. Another application is understanding the nonlinear behavior of wind turbines (due to e.g. nonlinear damping) [9]. When it comes to future solutions, there has been increasing interest in exploiting nonlinearity to create structures that are light and stiff simultaneously. Hence, it is not surprising that an increasing number of researchers are working to extend linear vibration analysis and testing methods to nonlinear structures. The following two subsections review some key features of nonlinear dynamic systems and the existing literature on nonlinear system identification.

1.1 Nonlinear Oscillating Structures

Linear vibration analysis is well established in the literature [10]. The equation of motion (EOM) describing such structures is illustrated in Eq. (1a). Matrices $\mathbf{M}$, $\mathbf{C}$, and $\mathbf{K}$ occurring there represent,

respectively, the distributions of mass, linear viscous damping and stiffness, while vector $\mathbf{x}(t)$ is the time response of the system subjected to the applied force $\mathbf{f}(t)$.

$$\mathbf{M}\ddot{\mathbf{x}} + \mathbf{C}\dot{\mathbf{x}} + \mathbf{K}\mathbf{x} = \mathbf{f}(t) \tag{1a}$$

$$\mathbf{M}\ddot{\mathbf{x}} + \mathbf{C}\dot{\mathbf{x}} + \mathbf{K}\mathbf{x} + \mathbf{f}_{nl}(\mathbf{x}, \dot{\mathbf{x}}) = \mathbf{f}(t), \tag{1b}$$

A detailed description of linear vibration theory is not the focus of this work (the interested reader may consult [10] for further details), but a few basic characteristics will be briefly reviewed. The steady-state forced response of a linear single-degree-of-freedom (SDOF) equation of motion is governed by two modal parameters: the linear natural frequency (ω_{lin}) and damping ratio (ζ_{lin}). A typical linear forced response is shown in Fig. 1 and these two linear parameters are marked in there as dashed horizontal lines, which implies that they are constant (or amplitude-independent) quantities. (The horizontal line corresponding to the natural frequency is sometimes called the Linear Normal Mode, or LNM.) Furthermore, due to this invariance, the linear frequency response is almost symmetric with respect to the Linear Normal Mode, as is also depicted in Fig. 1.

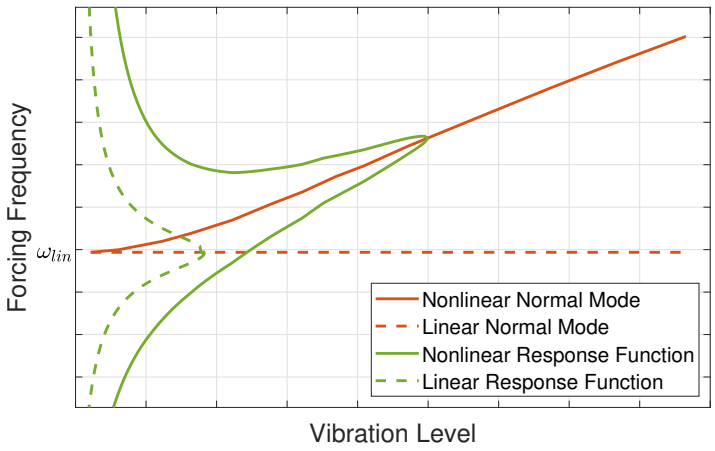

(a) Frequency vs. vibration amplitude

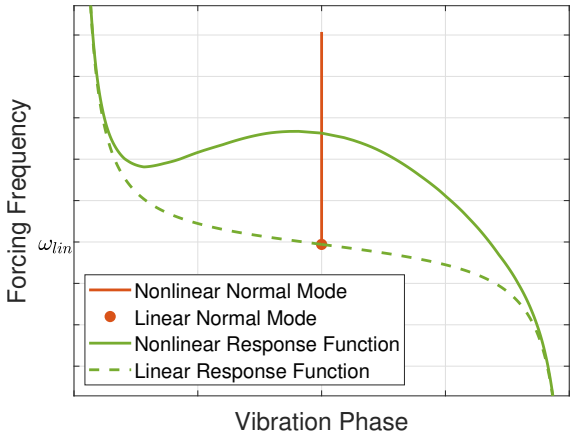

(b) Frequency vs. vibration phase

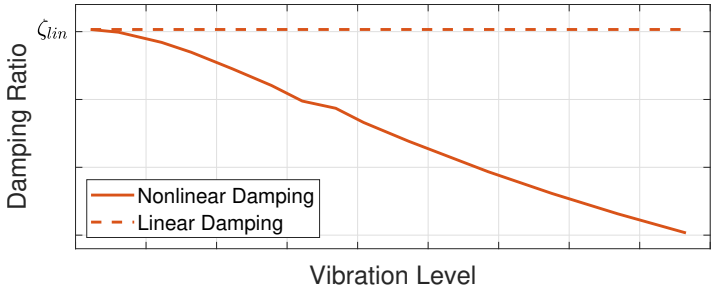

(c) Damping ratio vs. vibration amplitude

Fig. 1: Linear vs. nonlinear characteristics exhibited by general single-degree-of-freedom (SDOF) structures.

A general form of the equation of motion describing nonlinear structures is presented in Eq. (1b). It differs from the linear EOM by the additional vector function $\mathbf{f}_{nl}(\mathbf{x}, \dot{\mathbf{x}})$ that appears on the left

hand side of the equation and represents the nonlinearities present in the system. Because of these nonlinear terms, the resonance frequency and effective damping of the structure tend to change with vibration amplitude – as is also illustrated in Fig. 1(a) and 1(c), respectively. (Analogous to what mentioned in the previous paragraph – the natural frequency expressed as a function of vibration level is called a Nonlinear Normal Mode, or simply NNM [11].) This frequency-amplitude dependency causes the nonlinear Response Functions to lose symmetry (as shown in Fig. 1a), although they are still roughly centered on the NNM.

Most mechanical systems reveal their nonlinear nature only when they oscillate at sufficiently high amplitudes. Hence, their motion can be still approximated as linear if the vibrations are small enough. This is also illustrated in Fig. 1, where the Linear Normal Mode is shown to be tangent to its nonlinear counterpart when the vibration level approaches zero. Analogously, the linear damping ratio meets the nonlinear damping curve at low amplitudes. However, it is worth noting that not all systems have this characteristic, e.g. [12] presents an interesting exception.

The description above only highlights a few features that are important and should be taken into consideration while studying the dynamics of nonlinear structures, but it certainly does not cover all the phenomena occurring in these systems. The readers interested in investigating linear and nonlinear vibration in more detail could refer to [10] and [13–15], respectively.

1.2 White, Black and Grey Box System ID Algorithms

There are multiple ways to classify nonlinear system identification techniques. They could be grouped based on the domain they operate in, or the model function they are using. In this section, system identification methods are divided into three groups: white-, black- and gray-box algorithms. A brief description is provided below, together with a few examples of popular and state-of-art representatives of these three categories.

White-box identification procedures are based on well-understood physical laws expressed explicitly with functions that are known beforehand. These methods can be further divided into sub-groups based on the approach they take to identify the system, or the domain they operate in. Hence, one can distinguish *time-domain*, *frequency-domain* and *modal* methods.

Time- and *frequency-domain* white-box methods try to fit a differential equation (known a priori) to the measured signals in order to estimate the values of certain physical parameters that occur in that equation. A very popular choice for the identification in the former domain is the Restoring Force Surface (RFS) method. In [16] and [17], it have been proved successful in identifying mechanical systems exhibiting softening-stiffening and pure stiffening characteristics, respectively. Representatives of *frequency-domain* methods are Nonlinear Identification through Feedback of the Outputs (NIFO) and Nonlinear Identification through eXtended Outputs (NIXO). They were successfully applied to both numerical and real-life structures in [18–20] (NIFO) and [21,22] (NIXO). When the system is unforced, the FREEVIB method [23] has also proven very successful, although for many structures it is difficult to obtain free response measurements at sufficiently high amplitudes to use FREEVIB or other similar approaches.

On the other hand, *modal methods* try to directly identify the modal characteristics of a nonlinear system, such as Nonlinear Normal Modes (NNMs) or nonlinear damping ratio curves. The most popular methods of this type are the CONCERTO[1] [24], RCT[2] [25] and, inverse SNRM-based[3] [26]

[1]CONCERTO – COde for Nonlinear identifiCation from mEasured Response To vibratiOn

[2]RCT – Response-Controlled Stepped-Sine Testing

[3]inverse SNRM-based method – inverse Single Nonlinear Resonant Mode based method

algorithms. They all use the Single Nonlinear Resonant Mode (SNRM) formula [27] to model the nonlinearity present in the system. These methods are generally limited to systems in which a single mode is dominant, and have not yet been extended to cases where multiple modes of the linearized system interact.

In *black-box* identification, the model function is not known beforehand. In the early stages of this type of modeling, the researchers assume a general form of the function that will capture the physical phenomena present in the system, or they use a mathematical model limited by very few constraints. The final form of this model function crystallizes during the identification process based on the knowledge learned from monitoring the measured data or via machine learning techniques.

Some popular black-box identification methods were proposed and evaluated by Worden et al. in [28] and [29]. In the former work, the authors have proposed a time-domain technique called NARX (from Nonlinear Auto-Regressive with eXogenous inputs model) supported by a certain genetic algorithm. They employed it in black-box identification of a nonlinear equation of motion with a quadratic term. In [29], they compared the effectiveness of NARX, local models and recurrent neural networks in the black-box ID process of the signals obtained using a real-life tribometer. The analysts agree so far that black-box techniques can be considered powerful and find application in system ID of wide range of systems (because of their undefined nature). However, these algorithms simultaneously suffer from a rapid increase in the number of parameters to estimate (due to a general form of equations they utilize), and thus very large amounts of data may be needed in the identification, limiting their applicability.

Recently proposed black-box identification techniques lean towards a *data-driven* approach, which stands for the estimation of the investigated model based on the data captured in experiments without having prior knowledge regarding the mechanical system. One of the more popular methods was proposed by Moore, who employed his Characteristic Nonlinear System Identification (CNSI) method to identify an assembly consisting of a linear structure connected to a nonlinear energy sink [30], or in a different paper with multiple nonlinear attachments [31]. Another example of the data-driven approach (supported by the deep neural networks) was lately introduced by Li and Yang [32]. They managed to successfully identify the NNM of the Duffing equation [33] using response data only.

Finally, *grey-box* techniques combine both the learning from the measured data and a prior (usually partial) knowledge of the mechanical system. Gray-box modeling has certain advantages over its white-box and black-box siblings. The main benefit over the latter, is an opportunity to predict the situations not entirely covered by the measured data, or when parts of the collected data has low quality. Comparing with white-box models, the main improvement is the ability to model complex mechanical systems, that are not fully captured by the assumed governing formulas.

In [29], Worden et al. presented a successful attempt to identify a frictional system using the gray-box techniques based on the exponential Stribeck equation supported by the Lu-Gre and Generalized Maxwell Slip friction models. Noël, Kerschen, et al. investigated a concept of representing the complex stiffness and damping non-linear phenomena using cubic splines (piecewise third-order polynomials). They successfully employed their idea to capture the non-linear dynamics of solar arrays [34]. An interesting combination of the data-driven identification approach using the Gaussian function supported by partial knowledge of the system was recently proposed by Zhang and Cross [35].

1.3 Objectives and Contributions

The objective of this article is to introduce a novel technique for identifying black-box systems with geometric nonlinearity. Building upon the work presented in [22], we propose two frequency-domain system ID algorithms called D1-NIXO and D2-NIXO. In [22], a white-box version of NIXO proved successful in identifying parameters for a few geometrically nonlinear mechanical systems. In each case the equation of motion was assumed to be known and NIXO had only to identify the parameters. In this study, we extend this technique to a black-box identification method, which is applicable in cases where the nonlinear equation of motion that describes the structure's dynamics is not known a priori. Instead, a very general equation of motion is specified and the algorithm seeks to determine which terms are needed to describe the system in question.

The identification with the black-box version of NIXO consists of four steps: (*i*) postulating a general form of the nonlinear equation of motion that describes the dynamics of the structure (e.g. a geometrically nonlinear EOM where the nonlinearity represented with every possible quadratic, cubic, quartic, etc. polynomial term), (*ii*) performing an identification attempt using NIXO, (*iii*) detecting which nonlinear terms are dominant (and should be kept in the nonlinear EOM), and (*iv*) identifying the object one more time – this time using the EOM obtained after Step 3.

In Step 3, the division into the dominant and irrelevant terms is made based on the values of two metrics Δ_* and Δ_{**}, that are particular to NIXO and will be defined in Section 3 of this work. In essence, these metrics arose when NIXO was applied to several case studies and an interesting pattern was revealed. Namely, it was observed that if the tested structure: (*i*) was excited with a swept-sine forcing signal and (*ii*) oscillated at low (yet sufficiently high) amplitudes during the experiment, then the nonlinear terms that are not dominant in the system's response tend to be complex-valued. The above-mentioned Δ-metrics capture whether each parameter is mostly complex- or real-valued.

The following sections present the proposed NIXO-based black-box identification procedure and demonstrate the technique numerically and experimentally. The numerical case studies evaluate the algorithm under perfect conditions (the noise-free signals). The outcomes obtained there are used to generate the Nonlinear Normal Mode that is further compared to the NNM of the actual numerical structure. In the experimental case study, the identification attempt is performed on a 3D-printed beam and the results are validated against experimental measurements collected during swept-sine vibration testing, allowing the reader to see the limits of the applicability of this black-box identification procedure for the structures studied here.

The following section presents the overview of the NIXO method itself, while Section 3 elaborates on the black-box NIXO-based system identification process. In Section 4, the technique is evaluated in simulated experiments by applying it to an ICE-ROM [3] of a curved beam, and the outcomes are validated and discussed. Section 5 illustrates the results from the identification attempt performed on a beam 3D-printed from polylactide acid. Finally, Section 6 presents conclusions and future work.

2 An Overview of the NIXO Method

Nonlinear Identification through eXtended Outputs (NIXO) is a novel system identification algorithm that operates in the frequency domain. A detailed derivation of the method is presented in [22], along with its application to case studies where the modal equation of motion (EOM) is known beforehand. Since the derivation of NIXO is quite lengthy, this section provides only a brief overview of the method. All of the steps described here were implemented in Matlab ®.

For clarification purposes, let us assume that an equation of motion of a geometrically nonlinear single degree of freedom (SDOF) system is explicitly known and represented by Eq. (2).

$$\underbrace{m\ddot{x} + c\dot{x} + kx}_{\text{linear part}} + \underbrace{k_2x^2 + k_3x^3 + k_4^4 + k_5x^5}_{\text{nonlinear part}} = f(t) \tag{2}$$

This auxiliary equation will be utilized in this section to provide a simplified explanation of the system identification process using NIXO.

Furthermore, let us assume that the mass of the SDOF system is known and is equal to 1 ($m = 1$). Therefore, the equation of motion (2) consists of a linear part (with unknown linear damping and stiffness coefficients: c and k, respectively) and a nonlinear part represented by a quintic polynomial with four unknown stiffness coefficients: k_2, k_3, k_4, and k_5. The objective of NIXO is to estimate the values of c, k, k_2, k_3, k_4, and k_5 based on the system response.

The method is derived by first bringing the equation of motion (EOM) into the frequency domain using Fourier Transform, resulting in Eq. (3):

$$D(\Omega)X(\Omega) + k_2P_1(\Omega) + k_3P_2(\Omega) + k_4P_3(\Omega) + k_5P_4(\Omega) = \Psi(\Omega), \tag{3}$$

where Ω is the forcing frequency, and $X(\Omega)$, $P_i(\Omega)$, and $\Psi(\Omega)$ are the Fourier representations of the linear output, four nonlinear outputs, and forcing signal, respectively. (Naturally, $X(\Omega) = \mathcal{F}\{x(t)\}$, $P_i(\Omega) = \mathcal{F}\{x^{i+1}(t)\}$, and $\Psi(\Omega) = \mathcal{F}\{f(t)\}$, where the Fourier operator is denoted by $\mathcal{F}\{\cdot\}$, and $i \in \{1, 2, 3, 4\}$.) $D(\Omega)$ is the dynamic stiffness, which is the reciprocal of the frequency response function, H(Ω), whose explicit mathematical forms are provided in Eqs. (4) and (5), respectively.

$$D(\Omega) = -m\Omega^2 + ic\Omega + k \overset{m=1}{=\!=} -\Omega^2 + ic\Omega + k \tag{4}$$

$$H(\Omega) = \frac{1}{D(\Omega)} = \frac{1}{-\Omega^2 + ic\Omega + k} \tag{5}$$

Equation (3) assumes that the frequency-domain quantities presented therein are obtained by taking the fast Fourier transform (FFT) of their time-domain counterparts. In practice, it is beneficial to break each of these time signals into several overlapping pieces and apply a Hann window to each signal. For instance, matrices $\mathbf{X}$, $\mathbf{\Psi}$, and $\mathbf{P}_i$ ($i \in \{1, 2, 3, 4\}$) can be constructed using the matrix form presented in either Eq. (6) or Eq. (7).

$$\begin{aligned} D(\Omega)\left[X_1, \ldots, X_{N_{avg}}\right] + k_2\left[P_{1,1}, \ldots, P_{1,N_{avg}}\right] + k_3\left[P_{2,1}, \ldots, P_{2,N_{avg}}\right] + \\ + k_4\left[P_{3,1}, \ldots, P_{3,N_{avg}}\right] + k_5\left[P_{4,1}, \ldots, P_{4,N_{avg}}\right] = \left[\Psi_1, \ldots, \Psi_{N_{avg}}\right] \end{aligned} \tag{6}$$

$$D(\Omega)\mathbf{X}(\Omega) + k_2\mathbf{P}_1(\Omega) + k_3\mathbf{P}_2(\Omega) + k_4\mathbf{P}_3(\Omega) + k_5\mathbf{P}_4(\Omega) = \mathbf{\Psi}(\Omega), \tag{7}$$

where matrices $\mathbf{X}$, $\mathbf{\Psi}$, and $\mathbf{P}_i$ ($i \in \{1, 2, 3, 4\}$) have a size of $1 \times N_{avg}$, where N_{avg} is the number of blocks that the time signals have been split into.

The left-hand and right-hand sides of Eq. (7) should be divided by N_{avg} and then post-multiplied by either $\mathbf{X}^H$ or $\mathbf{\Psi}^H$, where $(\cdot)^H$ denotes the Hermitian or conjugate transpose operator. This results in obtaining Eqs. (8a) and (8b), respectively. Anticipating the rest of this section, Eq. (8a) will be further transformed into the $\mathbf{D}_1$-based NIXO base function, while Eq. (8b) will serve as the base

for the $\mathbf{D}_2$-NIXO system identifier. The difference between the $\mathbf{D}_1$-based and $\mathbf{D}_2$-based NIXO will be explained later in this section.

$$\frac{1}{N_{avg}}\left(D(\Omega)\mathbf{X}\mathbf{X}^H + k_2\mathbf{P}_1\mathbf{X}^H + k_3\mathbf{P}_2\mathbf{X}^H + k_4\mathbf{P}_3\mathbf{X}^H + k_5\mathbf{P}_4\mathbf{X}^H \right) = \frac{1}{N_{avg}}\mathbf{\Psi}\mathbf{X}^H \tag{8a}$$

$$\frac{1}{N_{avg}}\left(D(\Omega)\mathbf{X}\mathbf{\Psi}^H + k_2\mathbf{P}_1\mathbf{\Psi}^H + k_3\mathbf{P}_2\mathbf{\Psi}^H + k_4\mathbf{P}_3\mathbf{\Psi}^H + k_5\mathbf{P}_4\mathbf{\Psi}^H \right) = \frac{1}{N_{avg}}\mathbf{\Psi}\mathbf{\Psi}^H \tag{8b}$$

The term $\mathbf{\Psi}\mathbf{X}^H$ represents a sum over all windowed time blocks, as shown in Eq. (9). When divided by N_{avg}, it provides an estimate for the power spectrum $S_{\Psi X}$ (also defined in Eq. (9)) between the quantities $\mathbf{\Psi}$ and $\mathbf{X}$. Similarly, power spectra S_{XX}, $S_{\Psi\Psi}$, $S_{X\Psi}$, S_{P_iX}, and $S_{P_i\Psi}$ (where $i \in \{1,2,3,4\}$) can be obtained using the same method.

$$\frac{1}{N_{avg}}\mathbf{\Psi}\mathbf{X}^H = \frac{1}{N_{avg}}\left(\sum_{j=1}^{N_{avg}} \Psi_j X_j^H\right) = S_{\Psi X} \tag{9}$$

Therefore, Eqs. (8a) and (8b) can be equivalently expressed in the form presented in Eqs. (10a) and (10b), respectively.

$$D(\Omega)S_{XX} + k_2S_{P_1X} + k_3S_{P_2X} + k_4S_{P_3X} + k_5S_{P_4X} = S_{\Psi X} \tag{10a}$$

$$D(\Omega)S_{X\Psi} + k_2S_{P_1\Psi} + k_3S_{P_2\Psi} + k_4S_{P_3\Psi} + k_5S_{P_4\Psi} = S_{\Psi\Psi} \tag{10b}$$

Please note that Eqs. (8) and Eqs. (10) are valid for every individual frequency line. This means that the quantities $S_{\Psi X}$, S_{XX}, $S_{\Psi\Psi}$, $S_{X\Psi}$, S_{P_iX} (where $i \in \{1,2,3,4\}$) are actually functions of frequency. In equation (10), these functions could be presented as $S_{\Psi X}(\Omega)$, $S_{XX}(\Omega)$, $S_{\Psi\Psi}(\Omega)$, and so on, but the argument of these functions was not shown for clarity.

To identify a nonlinear structure, NIXO must solve a relatively large system of linear equations in the form of $\mathbf{A}\mathbf{u} = \mathbf{b}$. Here, $\mathbf{u}$ represents the vector of unknowns, and $\mathbf{A}$ and $\mathbf{b}$ represent the matrix and right-hand-side vector of known coefficients, respectively. Figure 2 illustrates the NIXO base formula used for this purpose.

The algebraic problem in Fig. 2 can be described by three quantities:

- The parameter p represents the number of nonlinear terms in the equation of motion, which is usually not more than a dozen. In the case of Eq. (2), p is equal to 4.
- The parameter n represents the number of frequency lines, which is typically a couple of hundreds or thousands.
- The parameter r stands for the number of transient vibration tests performed to collect the data needed to create the NIXO-based formula. In previous case studies, NIXO worked well when r was equal to 2 [36, 37], but it is possible to have r greater than 2.

The size of matrix $\mathbf{A}$ is $(r \times n) \times (n + p)$, while the length of vector $\mathbf{u}$ is $r \times n$, as indicated in the diagram in Fig. 2. These two quantities are filled out with the calculated power spectra from Eq. (10), following a certain pattern (for more information regarding this pattern, please refer to

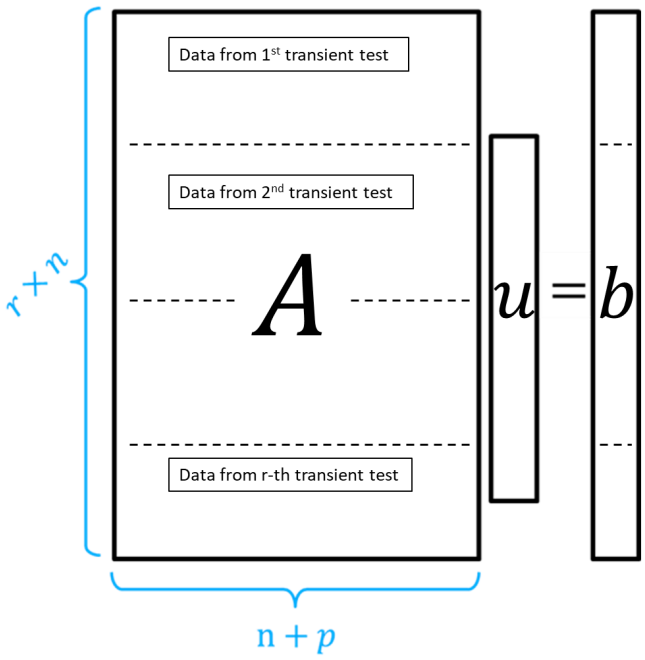

Fig. 2: A diagram illustrating the base formula used in the NIXO algorithm to identify nonlinear systems is shown below. p represents the number of nonlinear terms in the assumed equation of motion, n represents the number of frequency lines, and r represents the number of transient tests considered in a certain identification attempt.

publication [22]). The length of the unknown vector, $\mathbf{b}$, is $n + p$. Usually, the first n entries of this vector represent the dynamic stiffness (hence, they characterize the underlying linear part of the mechanical system), while the remaining p entries represent the unknown nonlinear coefficients. When equation of motion (2) is used, the value of p is 4, and the last four entries of vector $\mathbf{b}$ represent the unknown nonlinear coefficients: k_2, k_3, k_4, and k_5.

The rest of this section discusses three topics related to NIXO, which are listed below. It is necessary to elaborate on each of them as they address specific aspects of the black-box identification process presented in this work.

- The necessity of providing more than one input-output data set to NIXO.
- Differences between $\mathbf{D}_1$- and $\mathbf{D}_2$-based NIXO.
- Two variations of NIXO: one that estimates the nonlinear parameters as complex numbers and the other that finds them as real.

NIXO requires collecting data in at least two transient experimental tests. This data, which captures the response of the structure to the forcing signal, is needed to calculate the power spectra in Eq. (10). These calculations are used to populate matrix $\mathbf{A}$ and vector $\mathbf{b}$, which are key components of the NIXO-based system of equations presented in Fig. 2. This indicates that in cases where $r = 1$ and data is collected in only one transient experimental test, the NIXO-based system of equations cannot provide a unique solution because it is underdetermined. However, in cases where data is collected in multiple transient experimental tests ($r \geq 2$), the size of matrix $\mathbf{A}$ increases to$(r \times n) \times (n + p)$, resulting in a linear problem with more equations than unknowns.

This ensures that a unique solution exists. Recall that the value of n typically ranges from several hundred to several thousand, while p is no more than a dozen. This implies that from a practical standpoint, the inequality $(r \times n) > (n \times p)$ is always true.

Two variations of NIXO can be derived, referred to as $\mathbf{D}_1$-based and $\mathbf{D}_2$-based NIXO. The "$\mathbf{D}$" in these terms stands for dynamic stiffness, defined in Eq. (4), since NIXO estimates the linear part of the mechanical system in that form. The subscripts "1" and "2" indicate whether the cross-spectra are obtained via right-multiplying the equations of motion with the inputs or outputs, respectively. The $\mathbf{D}_1$-based NIXO linear problem presented in Fig. 2 is filled out with power spectra from Eq. (10a), while the $\mathbf{D}_2$-based NIXO formula uses power spectra from Eq. (10b).

The power spectra presented in Eq. (10) are generally complex numbers. This implies that the NIXO-based linear problem $\mathbf{Au} = \mathbf{b}$ can be classified as a system of complex linear equations. Therefore, the solution to such a system of equations will be a vector of complex numbers. The values of the nonlinear coefficients (k_2, k_3, k_4, and k_5), which were introduced as real numbers in Eq. (2), will also be estimated as complex. However, this has not been a major problem because if the identification process with NIXO is run correctly, the values of the nonlinear parameters are found as strongly real-valued[4]. Nonetheless, the issue of complex-valued nonlinear parameters can be overcome by estimating the real and imaginary parts of the unknown vector $\mathbf{u}$ separately (for more details, please refer to publication [22]). This modification enforces NIXO to find the nonlinear coefficients as real numbers. Lastly, the results obtained with the two versions of NIXO described in this paragraph are crucial for this publication. In Section 3, the nonlinear parameters estimated as complex numbers will be referred to as γ_{cmplx}, while those estimated as real numbers will be referred to as γ_{real}. These γ_{cmplx} and γ_{real} coefficients are further used to calculate the metrics Δ_* and Δ_{**}.

3 Proposed Black-Box NIXO Identification Procedure

This section provides a description of each of the four steps of the proposed procedure. Additionally, the diagrams in Fig. 3 support this description graphically.

In the first step, a general form of the nonlinear modal equation of motion is postulated. For example, Eq. (11) represents the modal EOM of a structure with geometric nonlinearity, and hence it consists of linear and nonlinear parts, where every possible quadratic and cubic stiffness term is assumed to occur. Please note that the hypothesis of proportional damping distribution is used to derive Eq. (11). This approach is commonly used for continuous nonlinear systems, which are examined in the numerical and experimental case studies presented in this work. Readers interested in learning about proportional damping in more detail could refer to [38, 39].

$$\underbrace{\ddot{q}_k + 2\zeta_k\omega_k\dot{q}_k + \omega_k^2 q_k}_{\text{linear part}} + \underbrace{\alpha_{11}^k q_1^2 + \alpha_{12}^k q_1 q_2 + \ldots}_{\text{quadratic part}} + \underbrace{\beta_{111}^k q_1^3 + \beta_{112}^k q_1^2 q_2 + \ldots}_{\text{cubic part}} = \mathbf{\Phi}_k^T \mathbf{f}(t) \tag{11}$$

To facilitate application to multi-degree-of-freedom systems, the expression in Eq. (11) describes the motion of the k-th mode of vibration, where $q_k(t)$ is the k-th modal coordinate, ω_k is the linear natural frequency, ζ_k – the linear damping ratio, and $\mathbf{\Phi}_k$ is the column vector representing the mass-normalized eigen-shape of the underlying linear and undamped mechanical system. One can

[4]The authors use the term "strongly-real-valued" to describe a complex number whose real part has a much larger magnitude than its imaginary part.

Step 1: Postulate a general form of the nonlinear EOM. For example:

$$\ddot{q}_k + 2\zeta_k\omega_k\dot{q}_k + \omega_k^2 q_k + \alpha_{11}^k q_1^2 + \alpha_{12}^k q_1 q_2 + \cdots + \beta_{111}^k q_1^3 + \beta_{112}^k q_1^2 q_2 + \cdots = \boldsymbol{\Phi}_k^T \boldsymbol{f}(t)$$

Step 2: Perform various swept-sine experimental tests, use measured input and output signals to form the NIXO-based algebraic problem, and solve this problem in order to identify the system.

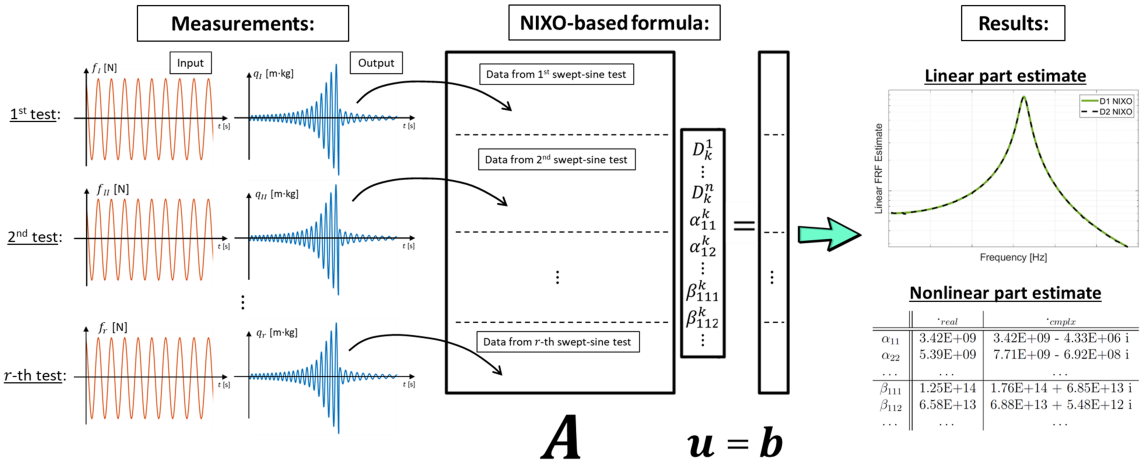

	$\cdot_{real}$	$\cdot_{cmplx}$
α_{11}	3.42E+09	3.42E+09 - 4.33E+06 i
α_{22}	5.39E+09	7.71E+09 - 6.92E+08 i
...	...	...
β_{111}	1.25E+14	1.76E+14 + 6.85E+13 i
β_{112}	6.58E+13	6.88E+13 + 5.48E+12 i
...	...	...

Step 3: Compute the Δ_* and Δ_{**} metrics to identify which nonlinear terms are dominant in the system, and which can be removed

	$Re\{\cdot_{cmplx}\}$	$Im\{\cdot_{cmplx}\}$	$\cdot_{real}$	Δ_* [%]	Δ_{**} [%]
α_{11}	3.42E+09	-4.33E+06	3.42E+09	0.16	99.87
α_{22}	7.71E+09	-6.92E+08	5.39E+09	43.14	91.03
...	...	...	...	...	...
β_{111}	1.76E+14	6.85E+13	1.25E+14	40.92	61.19
β_{112}	6.88E+13	5.48E+12	6.58E+13	1.51	99.18
...	...	...	...	...	...

Terms $\alpha_{11}q_1^2$ and $\beta_{112}q_1^2q_2$ are detected as dominant in the systems response, and should be kept in the EOM

Terms $\alpha_{22}q_2^2$ and $\beta_{111}q_1^3$ can be removed from the EOM

Step 4: Repeat system identification (as in step 2) on a reduced modal EOM found in step 3. If desired, the results can be evaluated by computing the Δ-metrics, or by comparing them to those obtained in step 2.

Reduced modal EOM considered in step 4: $\ddot{q}_k + 2\zeta_k\omega_k\dot{q}_k + \omega_k^2 q_k + \alpha_{11}^k q_1^2 + \beta_{112}^k q_1^2 q_2 = \boldsymbol{\Phi}_k^T \boldsymbol{f}(t)$

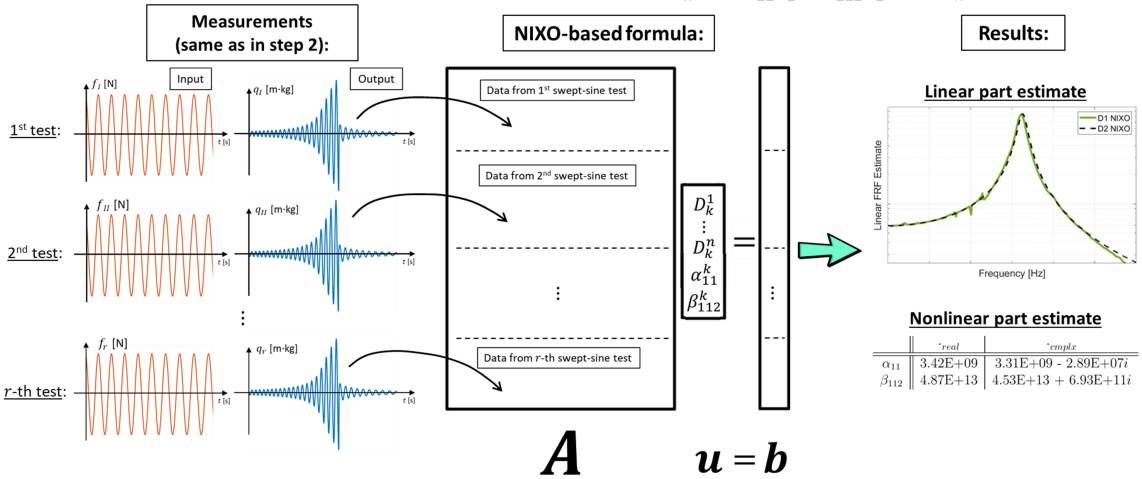

	$\cdot_{real}$	$\cdot_{cmplx}$
α_{11}	3.42E+09	3.31E+09 - 2.89E+07i
β_{112}	4.87E+13	4.53E+13 + 6.93E+11i

Final validation check of the identification results:

	$Re\{\cdot_{cmplx}\}$	$Im\{\cdot_{cmplx}\}$	$\cdot_{real}$	Δ_* [%]	Δ_{**} [%]	rel. difference between the results obtained in steps 2 and 4 [%]
α_{11}	3.31E+09	-2.89E+07	3.42E+09	3.15	99.13	1.16
β_{112}	4.53E+13	6.93E+11	4.87E+13	7.03	98.47	30.16

Term $\alpha_{11}q_1^2$ is most likely dominant and should be kept in the EOM

Term $\beta_{112}q_1^2q_2$ might not be dominant

Fig. 3: A diagram depicting the four steps involved in the system identification procedure using the black-box NIXO-based method.

account for as many modes as are present in the measurements, and the nonlinear terms account for any coupling between the modes as the vibration amplitude increases. Each modal equation contains several α_{uv}^k and β_{lmn}^k coefficients, corresponding to the nonlinear quadratic and cubic terms in the modal EOM. Their subscripts correspond to the product of polynomial terms that they multiply, for example: α_{uv}^k multiplies term $q_u q_v$, while the β_{lmn}^k term $q_l q_m q_n$. Finally, $\mathbf{f}(t)$ is the vector time function representing the force applied to the structure in the spatial domain.

In the second step, the parameters of the nonlinear system are identified with the NIXO method. In order to do so, one must first perform various swept-sine experimental test in which the structure vibrates at sufficiently distinguishable amplitudes, measure the input and output transient signals and provide them to the NIXO algorithm. NIXO then returns an estimate of the frequency response function of the underlying linear system, as well as the approximate values of the parameters for all nonlinear terms assumed beforehand. As already mentioned is Section 2, two different versions of NIXO are run, one of which estimates the parameters as complex numbers and the other that forces them to be real.

In the third step, one seeks to identify which nonlinear terms are dominant in the system, and which can be removed. The decision is made based on the values of two metrics (Δ_* and Δ_{**}), which are computed for each of the nonlinear α_{uv}^k- and β_{lmn}^k-coefficients found in Step 2. As already mentioned earlier in this section, the NIXO algorithm computes two estimates for each coefficient, one in which they are forced to be real valued, denoted γ_{real}, and another in which it is allowed to be complex, denoted γ_{cmplx}. (For clarity, the parameters α_{uv}^k- and β_{lmn}^k found as real and complex numbers are represented here with, respectively, γ_{real} and γ_{cmplx}.) The metrics in Eqs. (12) then measure the realness of the coefficients.

$$\Delta_* = \frac{\|\gamma_{real} - Re\{\gamma_{cmplx}\}\|}{\|\gamma_{real}\|} \tag{12a}$$

$$\Delta_{**} = \frac{\|\,|Re\{\gamma_{cmplx}\}| - |Im\{\gamma_{cmplx}\}|\,\|}{\|Re\{\gamma_{cmplx}\}\|} \tag{12b}$$

The nonlinear coefficients are considered to be dominant in the system if they are *strongly real-valued*. The metric Δ_* expresses the relative difference between the nonlinear coefficient that is forced to be real, and the real part of the complex one. In other words, it measures the consistency of the two above-mentioned identifications. The second metric, Δ_{**}, is defined as the relative difference between the real and imaginary parts of the complex solution. Hence, the nonlinear α_{uv}^k- and β_{lmn}^k-coefficients are considered to be *strongly real-valued* when: (i) Δ_* is a small number and (ii) Δ_{**} is close to 1.0. In this work, the criteria shown in Eq. (13) are used to identify coefficients that are dominant, since these criteria has proven successful based on past experience applying NIXO to experimental measurements and simulated data [36, 37]. If any of the α_{uv}^k- or β_{lmn}^k-coefficients satisfies both conditions simultaneously then it is considered to be significant in the modal equation of motion. Additionally, any terms that do not satisfy the criteria in Eqs. (13) are removed from the previously assumed modal EOM.

$$\begin{cases} \Delta_* \lesssim 10\% \\ \Delta_{**} \gtrsim 90\% \end{cases} \tag{13}$$

In Step 4, the system identification is repeated as in Step 2. However, rather than using the general modal EOM (11), the identification is performed on a reduced modal EOM that contains

only the dominant terms. The model thus obtained should be minimal and capture the behavior of the system well. If desired, one can further evaluate the results by computing the Δ-metrics again, or by comparing the nonlinear coefficients to those obtained in Step 2.

4 Black-box Identification with NIXO: Numerical Case Study

4.1 Numerical Test Description

This section illustrates black-box system identification by applying NIXO to a numerical model of a clamped-clamped curved beam. The structure is displayed in Fig. 4 and its geometric and mechanical properties are presented in Tab. 1.

Tab. 1: Geometric dimensions and mechanical parameters of the numerical curved clamped-clamped beam.

Length [mm]	Width [mm]	Thickness [mm]	Radius of curvature [m]
304.8	12.7	0.508	11.43

Young's modulus [Pa]	Density $\left[\frac{\text{kg}}{\text{m}^3}\right]$	Poisson's ratio
2.074×10^{11}	7870	0.29

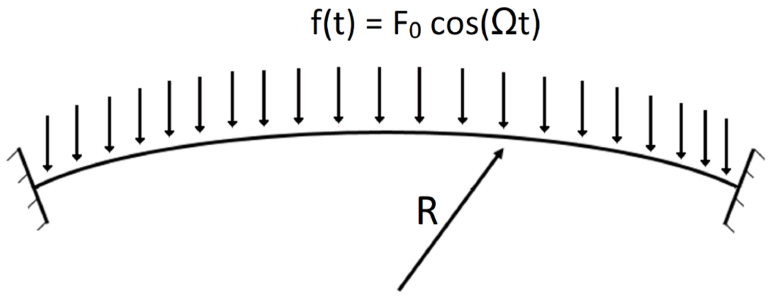

Fig. 4: The numerical model of a curved beam subjected to a uniformly distributed sinusoidal force.

The structure, modeled with 100 shell elements resulting in a total of 606 DOFs, is excited with a uniformly distributed sinusoidal force (Fig. 4). The finite element model (FEM) is used to generate the 3-mode ICE-ROM including the first three symmetric modes, i.e. modes 1, 3, 5. The modal equations of motion are presented in Eq. (14). Their nonlinear parts consists of 16 polynomial terms each, since they are represented with every possible quadratic and cubic polynomial term and (as mentioned above) the dynamics of the beam is modeled using 3 modes, where the indices 1, 2, 3 correspond to, respectively, modes 1, 3, and 5. The linear and nonlinear coefficients values are defined in Tables 2 and 3, respectively.

$$\ddot{q}_1 + 2\zeta_1\omega_1\dot{q}_1 + \omega_1^2 q_1 + \alpha_{11}^1 q_1^2 + \alpha_{12}^1 q_1 q_2 + \cdots + \beta_{111}^1 q_1^3 + \beta_{112}^1 q_1^2 q_2 + \cdots = \mathbf{\Phi}_1^T \mathbf{f}(t) \tag{14a}$$

$$\ddot{q}_2 + 2\zeta_2\omega_2\dot{q}_2 + \omega_2^2 q_2 + \alpha_{11}^2 q_1^2 + \alpha_{12}^2 q_1 q_2 + \cdots + \beta_{111}^2 q_1^3 + \beta_{112}^2 q_1^2 q_2 + \cdots = \mathbf{\Phi}_2^T \mathbf{f}(t) \tag{14b}$$

$$\underbrace{\ddot{q}_3 + 2\zeta_3\omega_3\dot{q}_3 + \omega_3^2 q_3}_{\text{linear part}} + \underbrace{\alpha_{11}^3 q_1^2 + \alpha_{12}^3 q_1 q_2 + \ldots}_{\text{quadratic stiffness part}} + \underbrace{\beta_{111}^3 q_1^3 + \beta_{112}^3 q_1^2 q_2 + \ldots}_{\text{cubic stiffness part}} = \mathbf{\Phi}_3^T \mathbf{f}(t) \tag{14c}$$

Tab. 2: Linear modal parameters of the numerical curved clamped-clamped beam.

Mode	ω_r [Hz]	ζ_r
1	65.181	0.0350
3	158.636	0.0262
5	385.882	0.0174

Tab. 3: Values of the polynomial coefficients in the nonlinear modal equations of motion (14). The values of coefficients α_{kl} and β_{lmn} have been obtained using a Matlab-based nonlinear FEA package, OSFern (https://bitbucket.org/cvandamme/osfern). The procedure in [40] was used to generate the nonlinear reduced order model (NLROM).

Parameter \ Mode		1	3	5
α_{11}		3.420E+09	1.961E+09	1.679E+09
α_{22}		6.403E+09	-1.222E+10	-1.843E+08
α_{33}	$\left[\frac{1}{\sqrt{\text{kg}}\ \text{m}^{3/2}\ \text{s}^2}\right]$	2.066E+10	-9.944E+09	-2.027E+10
α_{12}		3.873E+09	1.299E+10	-6.836E+09
α_{13}		2.022E+09	-6.202E+09	3.631E+10
α_{23}		-5.368E+09	-3.026E+08	-2.360E+10
β_{111}		2.017E+13	2.276E+13	1.576E+13
β_{112}		6.738E+13	1.903E+14	-1.362E+13
β_{113}		3.557E+13	-1.793E+13	3.423E+14
β_{221}		1.870E+14	4.635E+14	1.091E+13
β_{222}	$\left[\frac{1}{\text{kg}\ \text{m}^2\ \text{s}^2}\right]$	1.524E+14	9.332E+14	-2.576E+14
β_{223}		-8.006E+11	-7.799E+14	2.557E+15
β_{331}		3.858E+14	3.710E+14	6.213E+14
β_{332}		3.761E+14	2.676E+15	-2.120E+15
β_{333}		2.052E+14	-7.077E+14	6.639E+15
β_{123}		-1.792E+13	-2.868E+13	6.289E+14

This section presents the identification of the first nonlinear normal mode (NNM). Hence, the beam is excited near this mode using various up- and down-swept-sines, such that it oscillates at sufficiently different amplitudes in every test. The sweeps are 300-second-long and cover the frequency range from 1 to 115 Hz. This range of frequencies is chosen because the linear first mode is at approximately 65 Hz, and the sweep excitation in this range can capture increases and decreases in this mode's first natural frequency. The sweep rate is 0.38 Hz/s and is common to every numerical test run. The time signals are recorded using a sample increment of $\Delta t = 4.0 \times 10^{-4}$ s. The specifications of the input swept-sine signals are summarized in Tab. 4.

Tab. 4: Specification of the swept-sine forcing functions used to excite the numerical beam.

F_0 [N]	$[\Omega_{st},\ \Omega_{end}]$ [Hz]	t_{st} [s]	t_{end} [s]	$\Delta\Omega$ [Hz/s]	Δt [s]
various values (see legend in Fig. 5)	[1, 115] (up-sweep) [115, 1] (down-sweep)	0	300	0.38	4.0×10^{-4}

As illustrated in Fig. 5, the structure is excited with 17 different swept-sines. The modal signals $\mathbf{q}(t)$ are obtained via applying the transformation presented in Eq. (15) to the output signals measured in the physical domain, $\mathbf{x}(t)$.

$$\begin{bmatrix} q_1 \\ q_2 \\ q_3 \end{bmatrix} = \mathbf{\Phi}^{\dagger} \begin{bmatrix} x_1 \\ \vdots \\ x_{606} \end{bmatrix}, \tag{15}$$

where $\mathbf{\Phi}^{\dagger}$ represents the pseudo-inverse of the mass-normalized mode-shape matrix $\mathbf{\Phi}$.

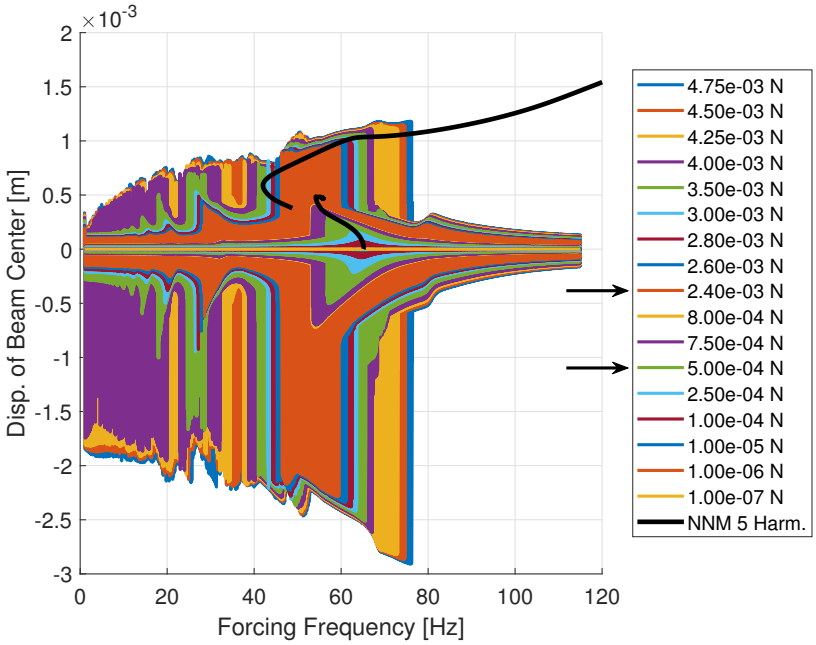

Fig. 5: The NNM curve overlayed on the swept-sine responses of varying amplitudes measured at the beam's center.

4.2 Set-up of the Black-Box System ID Procedure

The nonlinear part of the first modal EOM (of the clamped-clamped curved beam) is assumed to consists of every possible quadratic and cubic polynomial term. As a result, there are sixteen terms in this modal equation of motion, as presented in Eq. (14a).

The seventeen i/o signals were first grouped into different pairs, and then provided to the NIXO algorithms in order to identify the structure. This approach worked well in multiple case studies performed previously [36, 37].

In order to avoid overwhelming the reader with too much data, this section presents only the results from one pair of signals. Namely, the results presented come from a case study where only

the two data sets of input-output signals, obtained with forcing amplitudes: 2.4×10^{-3} N (up-sweep) and 5.0×10^{-4} N (down-sweep), were used. These signals are marked in the legend in Fig. 5 with black arrows, and their specifications are provided in Tab. 5. (Two sets of input-output signals are required to obtain an over-determined system of equations in NIXO, as was explained in Section 2.) The beam oscillates at very different vibration amplitudes when these two input signals are used to excite the beam (see Fig. 5). The smaller of the two is sufficient to excite the noticeable softening nonlinearity, while the other one produces the output signal exhibiting stiffening. (For completeness, at the end of Section 4 we reconsider the other signals shown in Fig. 5 and discuss how the results presented here contrast with those obtained when different pairs of signals were used.)

Tab. 5: Specification of the swept-sine forcing function(s) used in the black-box identification attempt presented in this article.

F_0 [N]	$[\Omega_{st},\ \Omega_{end}]$ [Hz]	t_{st} [s]	t_{end} [s]	$\Delta\Omega$ [Hz/s]	Δt [s]
2.4×10^{-3}	[1, 115] (up-sweep)	0	300	0.38	4.0×10^{-4}
5.0×10^{-4}	[115, 1] (down-sweep)				

4.3 Steps 2 and 3 of the System ID Procedure

In Step 2, NIXO returns the estimates of the underlying linear frequency response function and all the nonlinear terms in Eq. (14a). Figure 6a shows a comparison between the true and found frequency response functions of the underlying linear system for both the $\mathbf{D}_1$- and $\mathbf{D}_2$-based NIXO algorithms. (In each case two sets of coefficients were found, one where they were allowed to be complex and one when they were forced to be real.) When it comes to the nonlinear part of the EOM, the estimated values of α- and β-polynomial coefficients are listed in Tab. 6. Based on the Δ-metrics, only four nonlinear terms (corresponding to coefficients α^1_{11}, α^1_{12}, β^1_{111} and β^1_{112}) are found to be dominant in the first modal equation of motion.

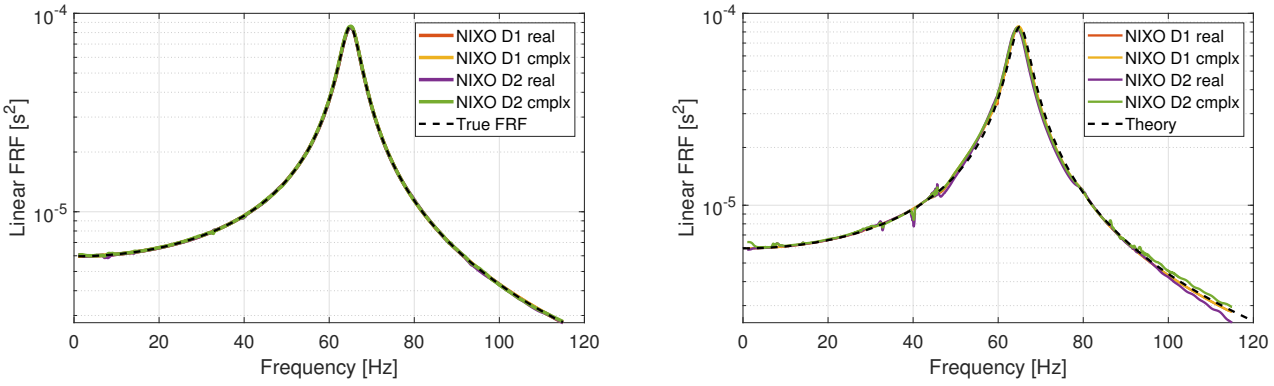

Fig. 6: Underlying linear system estimated by the NIXO algorithms in the **(a)** second and **(b)** fourth steps of the presented black-box identification procedure.

A few analyses were performed to verify that the four nonlinear terms identified by black-box NIXO are indeed dominant. First, the NNM curve computed for the estimated nonlinear EOM,

which contains only the four dominant terms and is presented in Eq. (16), is compared to the true NNM obtained for the EOM with the full set of 16 nonlinear terms, Eq. (14a).

$$\ddot{q}_1 + 2\zeta_1\omega_1\dot{q}_1 + \omega_1^2 q_1 + \alpha_{11}^1 q_1^2 + \alpha_{12}^1 q_1 q_2 + \beta_{111}^1 q_1^3 + \beta_{112}^1 q_1^2 q_2 = \mathbf{\Phi}_1^T \mathbf{f}(t) \tag{16}$$

To provide a visual comparison, Fig. 7 shows the two NNM curves described in the previous paragraph graphically. The NNM curves presented there were computed with the Multi Harmonic Balance (MHB) method [41–43] using the first five harmonics. The estimated NNM curve is marked there with a red solid line, and is obtained for the nonlinear parameter values from Tab. 6 returned by the $\mathbf{D}_1$-NIXO algorithm. The sixteen true nonlinear coefficient values from Tab. 3 were used to compute the "true" curve, shown with a blue solid line. As presented in Fig. 7, the estimated and target NNM curves match each other well until the vibrations amplitude exceeds twice the thickness of the beam (which is 0.508 mm). In contrast, if one computes the NNM using Eq. (17) and the true nonlinear coefficients (so excluding the four dominant ones), a straight vertical line (marked with green in Fig. 7) is obtained. In effect, those other 12 nonlinear terms shown in Eq. (17) contribute so little to the response that the mechanical system behaves linearly over this range of vibration amplitude. This is interesting, because Tab. 6 shows that it is not easy to distinguish the important terms from the others based on their magnitudes alone.

$$\begin{aligned}\ddot{q}_1 + 2\zeta_1\omega_1\dot{q}_1 + \omega_1^2 q_1 + \alpha_{22}^1 q_2^2 + \alpha_{33}^1 q_3^2 + \alpha_{13}^1 q_1 q_3 + \alpha_{23}^1 q_2 q_3 + \\ \beta_{113}^1 q_1^2 q_3 + \beta_{221}^1 q_2^2 q_1 + \beta_{222}^1 q_2^3 + \beta_{223}^1 q_2^2 q_3 + \beta_{331}^1 q_3^2 q_1 + \beta_{332}^1 q_3^2 q_2 + \beta_{333}^1 q_3^3 + \beta_{123}^1 q_1 q_2 q_3 = \mathbf{\Phi}_1^T \mathbf{f}(t)\end{aligned} \tag{17}$$

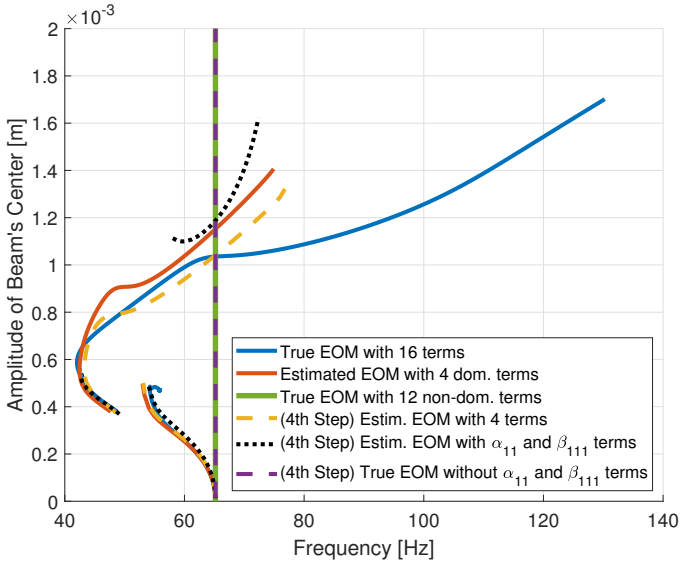

Fig. 7: A comparison of the true NNM curve to NNMs computed using the EOMs identified with the proposed NIXO-based procedure. The NNMs were computed with the Multi-Harmonic Balance method using the first five harmonics. Beam thickness: 0.508 mm.

Because the case study presented in this section is numerical, the true values of the nonlinear coefficients are known exactly, and they can also be used to further validate the findings of the algorithm. Table 7 compares the true values of the parameters α_{11}^1, α_{12}^1, β_{111}^1 and β_{112}^1 to their estimated values obtained with NIXO. The table shows that the relative difference between the true and estimated values is less than 3% and 5.5% for identification using $\mathbf{D}_1$-based and $\mathbf{D}_2$-based NIXO, respectively. The slightly less accurate results returned by $\mathbf{D}_2$-NIXO can be explained by its sensitivity to noise in the output signal.

Tab. 6: Estimated values of the nonlinear parameters obtained using the $\mathbf{D}_1$- and $\mathbf{D}_2$-based NIXO algorithms. Parameters marked with green satisfy the criteria (13), while those marked with blue are close to satisfying these requirements.

$\mathbf{D}_1$–NIXO		$Re\{\cdot_{cmplx}\}$	$Im\{\cdot_{cmplx}\}$	$\cdot_{real}$	Δ_* [%]	Δ_{**} [%]
α_{11}		3.42E+09	-4.33E+06	3.42E+09	0.16	99.87
α_{22}		7.71E+09	-6.92E+08	5.39E+09	43.14	91.03
α_{33}	$\left[\frac{1}{\sqrt{\text{kg}}\ \text{m}^{3/2}\ \text{s}^2}\right]$	9.84E+10	6.68E+10	3.18E+10	209.28	32.16
α_{12}		3.67E+09	2.38E+08	3.94E+09	6.89	93.51
α_{13}		5.17E+09	-2.51E+09	1.20E+09	331.44	51.41
α_{23}		3.42E+09	-1.51E+10	-4.56E+09	175.13	340.39
β_{111}		2.04E+13	1.68E+11	2.01E+13	1.51	99.18
β_{112}		6.88E+13	5.48E+12	6.58E+13	4.65	92.04
β_{113}		3.75E+13	-8.84E+13	5.77E+13	34.95	135.48
β_{221}		1.94E+14	1.45E+13	1.76E+14	10.55	92.54
β_{222}	$\left[\frac{1}{\text{kg}\ \text{m}^2\ \text{s}^2}\right]$	1.76E+14	6.85E+13	1.25E+14	40.92	61.19
β_{223}		-1.00E+15	-1.93E+15	2.07E+14	584.67	91.74
β_{331}		1.54E+15	-1.54E+15	9.56E+14	60.90	0.37
β_{332}		9.40E+15	-1.50E+16	3.32E+15	183.31	59.73
β_{333}		-4.31E+15	1.24E+16	5.18E+15	183.10	187.36
β_{123}		-1.01E+14	-8.46E+14	1.59E+14	163.83	735.67

$\mathbf{D}_2$–NIXO		$Re\{\cdot_{cmplx}\}$	$Im\{\cdot_{cmplx}\}$	$\cdot_{real}$	Δ_* [%]	Δ_{**} [%]
α_{11}		3.34E+09	-4.62E+07	3.44E+09	2.99	98.62
α_{22}		3.04E+09	1.95E+08	3.78E+09	19.62	93.59
α_{33}	$\left[\frac{1}{\sqrt{\text{kg}}\ \text{m}^{3/2}\ \text{s}^2}\right]$	1.58E+11	1.86E+10	8.66E+09	1722.15	88.23
α_{12}		4.29E+09	2.36E+08	3.73E+09	14.96	94.50
α_{13}		-1.31E+08	-3.81E+09	3.27E+09	104.02	2799.63
α_{23}		-3.76E+09	-2.42E+10	8.18E+09	145.96	544.40
β_{111}		1.94E+13	-4.71E+11	2.03E+13	4.71	97.57
β_{112}		6.47E+13	-2.59E+12	6.28E+13	3.00	95.99
β_{113}		3.22E+13	-4.39E+13	1.09E+14	70.59	36.56
β_{221}		1.54E+14	2.84E+12	1.36E+14	12.82	98.15
β_{222}	$\left[\frac{1}{\text{kg}\ \text{m}^2\ \text{s}^2}\right]$	2.17E+14	7.61E+13	2.81E+13	670.85	64.90
β_{223}		-2.76E+15	-1.06E+15	2.55E+14	1181.73	61.44
β_{331}		2.66E+15	-1.26E+15	2.21E+15	19.96	52.54
β_{332}		1.19E+16	-1.10E+16	1.17E+16	2.14	7.54
β_{333}		2.72E+16	-5.16E+15	6.01E+15	352.15	81.01
β_{123}		-2.02E+14	-5.40E+14	4.71E+14	143.02	166.71

4.4 Step 4 of the System ID Procedure

In this particular case study, the black-box identification results obtained after Step 3 are already satisfactory. However, the linear FRFs computed by NIXO are potentially influenced by all of the nonlinear terms, both dominant and non-dominant, so one should repeat the identification using EOM with only the dominant terms $\alpha^1_{11}q_1^2$, $\alpha^1_{12}q_1q_2$, $\beta^1_{111}q_1^3$, and $\beta^1_{112}q_1^2q_2$. This also serves to check

Tab. 7: Comparison of the true and estimated values of the four terms pointed out by NIXO.

Parameter \ Value		True	$\mathbf{D}_1$-NIXO Avg. estimate	$\mathbf{D}_1$-NIXO Rel. error [%]	$\mathbf{D}_2$-NIXO Avg. estimate	$\mathbf{D}_2$-NIXO Rel. error [%]
α_{11}	$\left[\frac{1}{\sqrt{\text{kg}}\ \text{m}^{3/2}\ \text{s}^2}\right]$	3.42E+09	3.42E+09	0.00	3.39E+09	0.88
α_{12}		3.87E+09	3.94E+09	1.81	4.01E+09	3.62
β_{111}	$\left[\frac{1}{\text{kg}\ \text{m}^2\ \text{s}^2}\right]$	2.02E+13	2.01E+13	0.49	1.99E+13	1.73
β_{112}		6.74E+13	6.58E+13	2.37	6.38E+13	5.42

that the values obtained for those four polynomial coefficients are not influenced by the terms that have been discarded.

The outcomes from Step 4 are presented in Fig. 6b and Tab. 8. Figure 6b shows that the estimate of the underlying linear system still matches the truth model, however a slight degradation can be observed. Apparently the discarded terms do affect the estimate of the linear FRF even though their influence is very small. When it comes to the nonlinear part of the structure, the estimated values of the α and β coefficients are presented in Tab. 8. It is worth noting that the Δ-metrics of all four coefficients obtained with $\mathbf{D}_1$-NIXO and three out of four returned by $\mathbf{D}_2$-NIXO satisfy the accuracy criteria in Eq. (13). Furthermore, comparing the values of the nonlinear parameters with those obtained in Step 2 reveals that only α^1_{11} and β^1_{111} values were consistent and were identified accurately relative to the true parameters. This makes one question whether the other two parameters are indeed important to the studied mechanical system's response.

To explore this, three additional NNM curves were computed and are presented in Fig. 7. The first NNM curve (marked with yellow dashed line) is the NNM for the EOM in Eq. (16) with the nonlinear coefficient values from Tab. 8. This NNM is still very close to the true one, even though the values of α^1_{12} and β^1_{112} are not very close to their true values. However, when the NNM is computed using EOM with only the polynomial terms $\alpha^1_{11}q_1^2$ and $\beta^1_{111}q_1^3$ (see Eq. (18)) with the average parameter values in Tab. 8, the black dotted line in Fig. 7 shows that the NNM is not quite as accurate as when the structure's nonlinearity is described with all four terms in Eq. (16). Even though there is considerable uncertainty in the values of α^1_{12} and β^1_{112}, the model appears to be slightly more accurate when they are included.

$$\ddot{q}_1 + 2\zeta_1\omega_1\dot{q}_1 + \omega_1^2 q_1 + \alpha^1_{11}q_1^2 + \beta^1_{111}q_1^3 = \mathbf{\Phi}_1^T\mathbf{f}(t) \tag{18}$$

The last NNM (purple dashed line in Fig. 7) uses Eq. (19), where the nonlinear part is described by all of the nonlinear terms except $\alpha^1_{11}q_1^2$ and $\beta^1_{111}q_1^3$. The nonlinear coefficients are assigned their true values from Tab. 3. The NNM for this case is also a straight line, further demonstrating that most of the nonlinearity in the first mode of this particular beam comes from $\alpha^1_{11}q_1^2$ and $\beta^1_{111}q_1^3$.

$$\begin{aligned}
&\ddot{q}_1 + 2\zeta_1\omega_1\dot{q}_1 + \omega_1^2 q_1 + \\
&\quad \alpha^1_{12}q_1q_2 + \alpha^1_{22}q_2^2 + \alpha^1_{33}q_3^2 + \alpha^1_{13}q_1q_3 + \alpha^1_{23}q_2q_3 + \\
&\quad \beta^1_{112}q_1^2q_2 + \beta^1_{113}q_1^2q_3 + \beta^1_{221}q_2^2q_1 + \beta^1_{222}q_2^3 + \beta^1_{223}q_2^2q_3 + \beta^1_{331}q_3^2q_1 + \beta^1_{332}q_3^2q_2 + \beta^1_{333}q_3^3 + \\
&\qquad \beta^1_{123}q_1q_2q_3 = \mathbf{\Phi}_1^T\mathbf{f}(t)
\end{aligned} \tag{19}$$

Tab. 8: Nonlinear parameters estimates obtained in Step 4 of the black-box identification procedure. The units of α and β coefficients are $\frac{1}{\sqrt{\text{kg}}\ \text{m}^{3/2}\ \text{s}^2}$ and $\frac{1}{\text{kg}\ \text{m}^2\ \text{s}^2}$, respectively.

$\mathbf{D}_1$–NIXO	$Re\{\cdot_{cmplx}\}$	$Im\{\cdot_{cmplx}\}$	$\cdot_{real}$	Δ_* [%]	Δ_{**} [%]	True	Avg. estim.	Rel. error [%]
α_{11}	3.31E+09	-2.89E+07	3.42E+09	3.15	99.13	3.42E+09	3.36E+09	1.68
α_{12}	3.18E+09	1.36E+08	2.92E+09	8.94	95.71	3.87E+09	3.05E+09	21.29
β_{111}	1.95E+13	-1.86E+11	2.06E+13	5.58	99.05	2.02E+13	2.01E+13	0.67
β_{112}	4.53E+13	6.93E+11	4.87E+13	7.03	98.47	6.74E+13	4.70E+13	30.28

$\mathbf{D}_2$–NIXO	$Re\{\cdot_{cmplx}\}$	$Im\{\cdot_{cmplx}\}$	$\cdot_{real}$	Δ_* [%]	Δ_{**} [%]	True	Avg. estim.	Rel. error [%]
α_{11}	3.11E+09	-3.35E+06	3.33E+09	6.45	99.89	3.42E+09	3.22E+09	5.84
α_{12}	2.99E+09	1.89E+08	1.66E+09	80.18	93.67	3.87E+09	2.32E+09	39.94
β_{111}	1.74E+13	-3.26E+10	1.91E+13	9.02	99.81	2.02E+13	1.82E+13	9.74
β_{112}	3.53E+13	1.23E+12	3.36E+13	5.20	96.53	6.74E+13	3.44E+13	48.90

4.5 Discussion

In summary, using the proposed black-box procedure, an EOM that initially consisted of 16 nonlinear terms was reduced to one containing only two or four that are the most dominant (depending on which step the algorithm is terminated). The other fourteen (or twelve) of the terms were found to contribute little to the response and were removed from the EOM. Discarding the nonlinear terms did introduce some errors into the linear FRF estimates, but they were quite small. The errors regarding the dominant nonlinear coefficients increased slightly from approximately 5.5% to less than 10%. As this case study showed, the number of dominant nonlinear terms is somewhat subjective as the true equation of motion that was used to generate the simulated measurements had many more terms than those that were found to be important.

The results shown so far pertain only to a pair of data sets of input-output signals specified in Tab. 5. Many other case studies, which are not reported here, were performed using various pairs of the signals displayed in Fig. 5.

Those studies revealed that if neither of the i/o signals used had large enough amplitude then fewer nonlinear terms estimated in Step 2 would satisfy criteria (13), and the nonlinear dynamics of the structure would definitely not be captured accurately during the accuracy check in Step 4. The other finding that resulted from the various case studies was that is the i/o signals used were of higher amplitude then more nonlinear terms would be detected in Step 3 as dominant in the system. However, the overall quality of such black-box identification would be lower than the one presented in this section (the one using signals from Tab. 5), since the objective here is to detect the smallest model that can capture the dynamics of the system.

It is also worth noticing that this section has focused on describing how to perform black-box identification with the minimum set of data (two pairs of input and output signals). In practice, it would probably be best to collect a surplus of data shown in Fig. 5, and then to use some of it for identification and other data for validation. This approach is commonly used in the machine learning community and has proven very effective. Future studies will explore this in more detail to understand what cross validation methodology yields the most accurate and reliable system identification.

Lastly, the case study presented in this section utilized noise-free signals generated numerically. The purpose of this study was to demonstrate the application of the NIXO-based black-box algorithm

for a relatively simple system. There is a wealth of literature that discusses the statistical properties of spectral estimators such as the H- and NIXO estimators that are used in this work, and the interested reader can infer much from these works about how NIXO might behave in the presence of noise [44]. In Section 5 the algorithm is applied to real-life experimental measurements that are affected by noise, and hence it gives a good indication of the potential obstacles that the black-box NIXO-based method may encounter in the presence of noise. Further theoretical studies of the effect of noise on NIXO and the black-box identification algorithm should be addressed in future research.

5 Black-box Identification with NIXO: Experimental Case Study

5.1 Experimental Test Description

The NIXO-based black-box identification procedure was applied to the signals measured on a 3D-printed flat beam with two accelerometers attached. A CAD drawing of the test structure and a photo of the test setup are shown in Fig. 8.

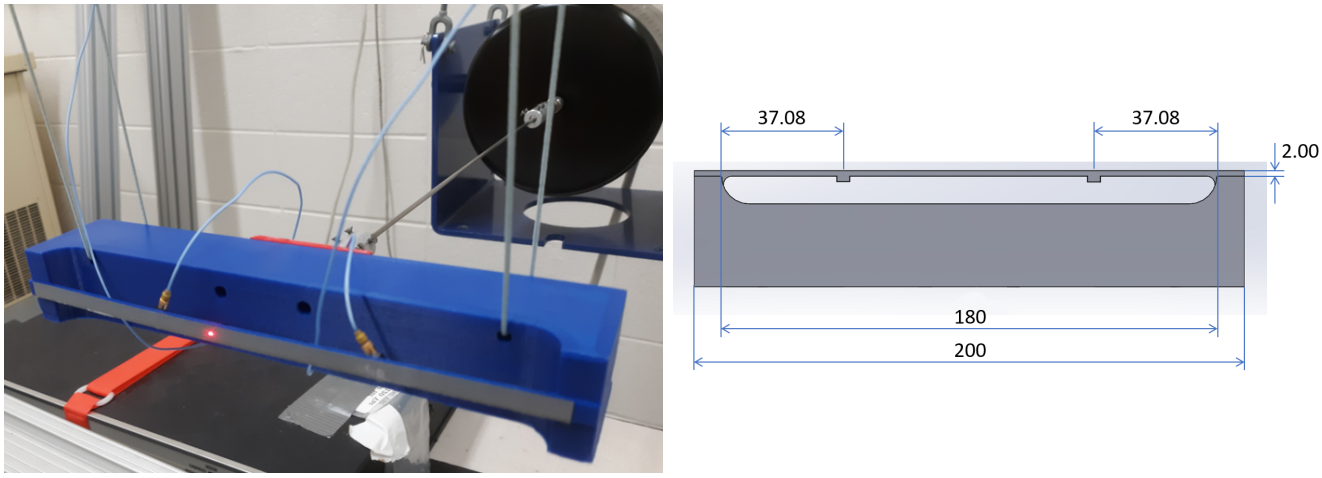

(a) **(b)**

Fig. 8: **(a)** A photograph of the experimental setup and **(b)** the longitudinal cross-section of beam model with the accelerometers attached.

The sample used in the experiment was 3D-printed using polylactide (PLA). It consists of two parts, thin and thick, that were printed as one unit and so are not-detachable from one another. In this work, these parts are referred to as beam and backing, respectively. This design prevents the beam's ends from slipping even when it oscillates at high amplitudes, which is an often-encountered circumstance when the ends of a beam are held in place using bolted joints (as was done in other similar systems [20]). While identifying nonlinearities due to bolted joints is very important in many industrial applications, this test structure was designed to focus only on the geometric nonlinearity. In future works, it would be interesting to use this approach on systems with frictional nonlinearity as well.

Table 9 summarizes the dimensions and mass of the 3D-printed sample and accelerometers. It is worth noting that the values displayed in Tab. 9 are nominal and subject to the variations inherent in the 3D printing process. Even though the beam itself is designed to be nominally flat, it

still could contain significant curvature due to manufacturing variation or thermal stress/expansion. The mechanical properties, such as Young's modulus or Poisson ratio, are also difficult to determine for the same reason. The natural frequency and damping ratio of two modes of the structure were identified by exciting the structure at very low amplitude, with the results shown in Fig. 9, and the values obtained are given in Tab. 10.

Tab. 9: Nominal dimensions and masses of the 3D printed sample and accelerometers.

	Length [mm]	Width [mm]	Thickness [mm]	Approx. mass [g]	Approx. mass of one accelerometer [g]
Beam	180	8	2	3.77	0.198
Backing	200	30	30	130.00	

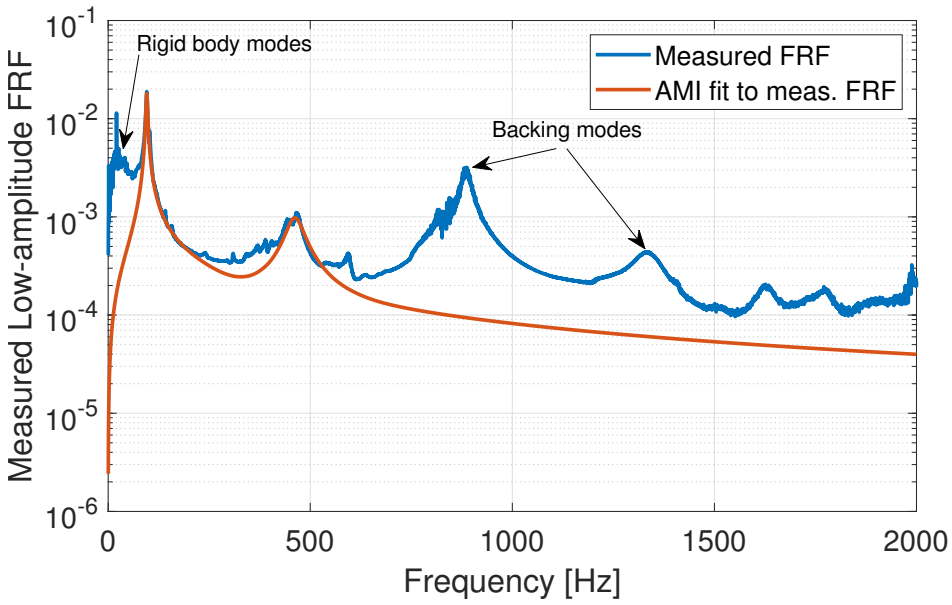

Fig. 9: Linear Frequency Response Function of the 3D-printed flat beam with the accelerometers attached. Fit to the first two modes in the FRF computed using the Algorithm of Mode Isolation (AMI) [45]. The peaks at 887.5 and 1337.0 Hz are modes of the backing.

Tab. 10: Linear modal properties of the flat beam-accelerometer assembly.

Mode ID	$\omega_{0,k}$ [Hz]	ζ_k	Mode shape
1	91.076	0.0119	1st bending of thin clamped-clamped beam
2	462.6952	0.0466	3rd bending of thin clamped-clamped beam (2nd symmetric bending)

The mass of the accelerometers is not negligible in this case study. Table 11 presents a comparison of the modal characteristics of the beam with and without the attached accelerometers. When the accelerometers were added, the natural frequencies of modes 1 and 3 are shifted by 6.37 Hz and 72.22 Hz, respectively. Additionally, the damping ratios of these modes were impacted

Tab. 11: Comparison of the modal characteristics of the 3D-printed beam with and without accelerometers attached.

	beam with accelerometers		beam without accelerometers					
k	ω_k [Hz]	ζ_k	ω_k [Hz]	ζ_k	$\Delta\omega_k$ [Hz]	$\Delta\zeta_k$	$\Delta\omega_k/\omega_k$ [%]	$\Delta\zeta_k/\zeta_k$ [%]
1	91.076	0.0119	97.446	0.0189	6.370	0.007	6.99	58.81
2	462.695	0.0466	534.919	0.0243	72.224	-0.022	15.61	-47.89

by the addition of accelerometers, with ζ_1 decreasing by approximately 58.81% and ζ_2 increasing almost twofold. These changes can be attributed to the mass of each accelerometer (0.198 g) in comparison to that of the thin beam (3.77 g), which shows that the former represents approximately 5.25% of the latter. The accelerometer cables likely also contribute to these differences, especially the damping.

A photograph of the experimental setup is shown in Fig. 8a. The backing was connected to the shaker via a steel stinger and the response was measured with a PSV-400 Scanning laser vibrometer (pointing at the beam's center) and with two PCB352C23 accelerometers located 37.08 millimeters from the beam's ends (see Fig. 8b). The shaker was a 100 lbf Modal Exciter Model 2100E11 powered by a 2050E05 Linear Power Amplifier. The voltage input signal sent to the shaker was generated by the Polytec software. Polytec was also used to collect the output velocity and acceleration signals coming from the vibrometer and accelerometers, respectively.

5.2 Conversion of the Input Voltage Signal into Distributed Force

Because the system of interest is a fixed-fixed beam, and not the assembly that includes the backing, it was necessary to convert the point force applied at the backing into an inertial load acting on the beam. This was done by assuming that the inertial force was uniformly distributed along the thin beam, and using the modal model to reconstruct the response to a uniform force $\mathbf{F} = F_{\text{mag}}[1, 1, 1]^{\text{T}}$ (see Fig. 10). The measured velocity in response to such a force is given by Eq. (20).

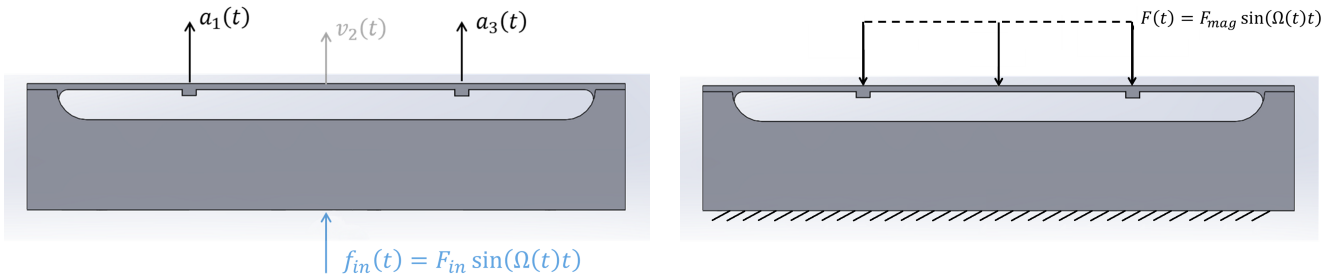

Fig. 10: The external point-force applied at the backing's center (shown in **(a)**) is converted into a force distributed along the length of the beam (shown in **(b)**).

$$\mathbf{V}_{lin}^{theory}(\Omega) = \sum_{k=1}^{N_{RB}} \frac{-\boldsymbol{\Phi}_k^{RB}\left(\boldsymbol{\Phi}_k^{RB}\right)^T \mathbf{F}}{\Omega} \quad + \quad \sum_{k=1}^{N_{lin}} \frac{\boldsymbol{\Phi}_k \boldsymbol{\Phi}_k^T \mathbf{F}\Omega}{\omega_{0,k}^2 - \Omega^2 + 2i\zeta_k\omega_{0,k}\Omega}, \tag{20}$$

where $\boldsymbol{\Phi}_k$ is k-th mass-normalized mode shape of the beam assembly, and $\boldsymbol{\Phi}_k^{RB}$ is the k-th mass-normalized rigid-body mode of the structure. Since the response of the system is measured at three physical points, the vectors $\boldsymbol{\Phi}_k$ have three rows, and the values of the identified mode shapes at these locations are given in Eq. (21). Note that to obtain the mode shapes the accelerometer measurements were integrated to obtain velocity.

$$\boldsymbol{\Phi} = [\boldsymbol{\Phi}_1, \boldsymbol{\Phi}_2] = \begin{bmatrix} 10.60 & 22.58 \\ 25.96 & -20.99 \\ 10.60 & 22.58 \end{bmatrix} \frac{1}{\sqrt{\text{kg}}} \tag{21a}$$

$$\boldsymbol{\Phi}^{RB} = \boldsymbol{\Phi}_1^{RB} = \begin{bmatrix} 8.633 \times 10^{-2} \\ 8.633 \times 10^{-2} \\ 8.633 \times 10^{-2} \end{bmatrix} \frac{1}{\sqrt{\text{kg}}} \tag{21b}$$

Then, the velocity at the center of the beam was measured experimentally and compared to a set of measurements with various voltages sent to the shaker $F_{in} \in \{0.010,\ 0.015,\ 0.025,\ 0.050\}$ volts. The force magnitude F_{mag} was then adjusted until the measurements overlaid with the model. An example of this comparison is presented in Fig. 11.

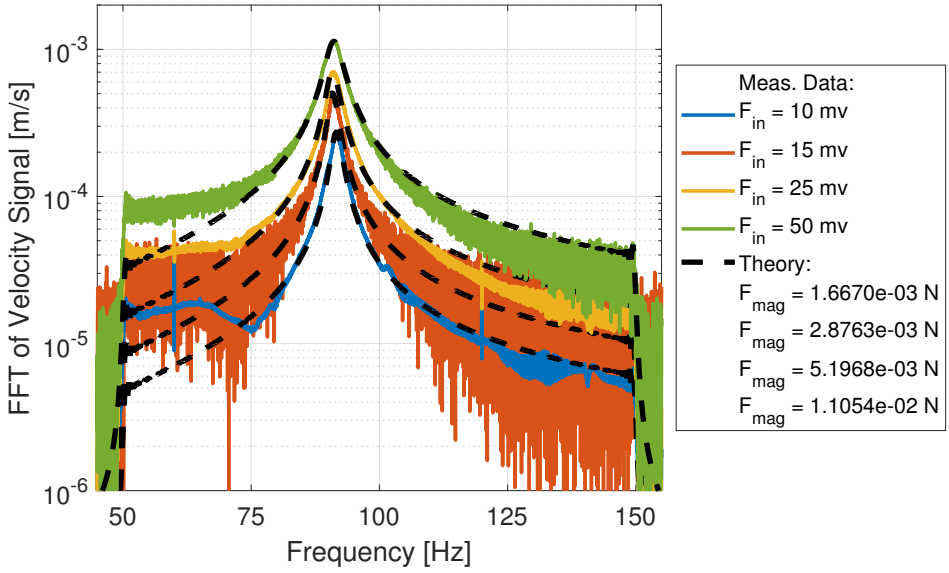

Fig. 11: FFT of the low-level velocity of the beam's center measured and obtained by the model in Eq. (20) near mode 1.

The values obtained for F_{mag} were $\{1.6670,\ 2.8763,\ 5.1968,\ 11.054\} \times 10^{-3}$ N. Hence, the correlation between the input voltage and force amplitudes was found to be $F_{mag} \approx 0.2343F_{in} - 6.5897 \times 10^{-4}$, where F_{mag} and F_{in} are expressed in newtons and volts, respectively. It is worth noting that the response functions shown in Fig. 11 exhibit slight frequency shifts even though the vibration amplitude was very low. Nevertheless, their responses were still modeled using Eq. (20) although with the parameters $\omega_{0,1}$ and ζ_1 adjusted slightly.

5.3 Black-box System ID Set-up: Experimental Case Study

When applying the proposed black-box identification procedure to this system, the general form of the equation of motion describing a geometrically nonlinear structure was again assumed, as shown in Eq. (22). Since the dynamics of the system is represented here with the two first symmetric modes, the nonlinear part of each modal equation of motion in Eq. (22) contains 7 polynomial terms.

$$\ddot{q}_1 + 2\zeta_1\omega_1\dot{q}_1 + \omega_1^2 q_1 + \alpha_{11}^1 q_1^2 + \alpha_{12}^1 q_1 q_2 + +\alpha_{22}^1 q_2^2 + \beta_{111}^1 q_1^3 + \beta_{112}^1 q_1^2 q_2 + \beta_{122}^1 q_1 q_2^2 + \beta_{222}^1 q_2^3 = \mathbf{\Phi}_1^T \mathbf{f}(t) \quad (22a)$$

$$\underbrace{\ddot{q}_2 + 2\zeta_2\omega_2\dot{q}_2 + \omega_2^2 q_2}_{\text{linear part}} + \underbrace{\alpha_{11}^2 q_1^2 + \alpha_{12}^2 q_1 q_2 + +\alpha_{22}^2 q_2^2}_{\text{quadratic stiffness part}} + \underbrace{\beta_{111}^2 q_1^3 + \beta_{112}^2 q_1^2 q_2 + \beta_{122}^2 q_1 q_2^2 + \beta_{222}^2 q_2^3}_{\text{cubic stiffness part}} = \mathbf{\Phi}_2^T \mathbf{f}(t) \quad (22b)$$

To identify nonlinear mode 1, the structure was subjected to nine swept-sine input signals of different magnitudes. Each of these linear up-sweeps was 204.8-second-long and covered a frequency range from 50 to 150 Hz. The measurements were recorded with a sample increment of $\Delta t = 3.9063 \times 10^{-4}$ s. The signals measured with the laser vibrometer and two accelerometers were then filtered and integrated in the frequency domain in order to obtain the velocity and displacement measurements presented in Fig. 12. Namely, the measured accelerations a_1 and a_3 in Fig. 10a were high-pass filtered with a Butterworth filter and integrated via dividing the FFT of the signals by $i\Omega$ to estimate velocity and again for displacement. The same approach was used to obtain the displacement from the laser vibrometer signal. Then Eq. (23) was used to obtain the modal coordinates $[q_1(t), q_2(t)]$ as a function of time.

$$\begin{bmatrix} q_1 \\ q_2 \end{bmatrix} = \mathbf{\Phi}^{\dagger} \begin{bmatrix} x_1 \\ x_2 \\ x_3 \end{bmatrix}, \quad (23)$$

where $\mathbf{\Phi}$ is defined in Eq. (21), and $(\dagger)$ denotes the pseudo-inverse.

The identification strategy used here was similar to that reported in Section 4. Namely, the input-output signals were paired with one another and then these pairs were provided to the NIXO algorithms. (As explained in Section 2, providing more than one set of input-output signals to NIXO is necessary to formulate a set of equations that has a unique solution.) The resultant 21 pairs are summarized in Table 12.

Tab. 12: Input-output signals are first grouped into 21 pairs and then provided to the NIXO algorithms.

Input signal voltage amplitude [mV]		
1st signal	2nd signal	# of pairs
50	{ 25}	1
100	{ 50, 25}	2
150	{100, 50, 25}	3
200	{150, 100, 50, 25}	4
250	{200, 150, 100, 50, 25}	5
300	{250, 200, 150, 100, 50, 25}	6
	Together:	21 pairs

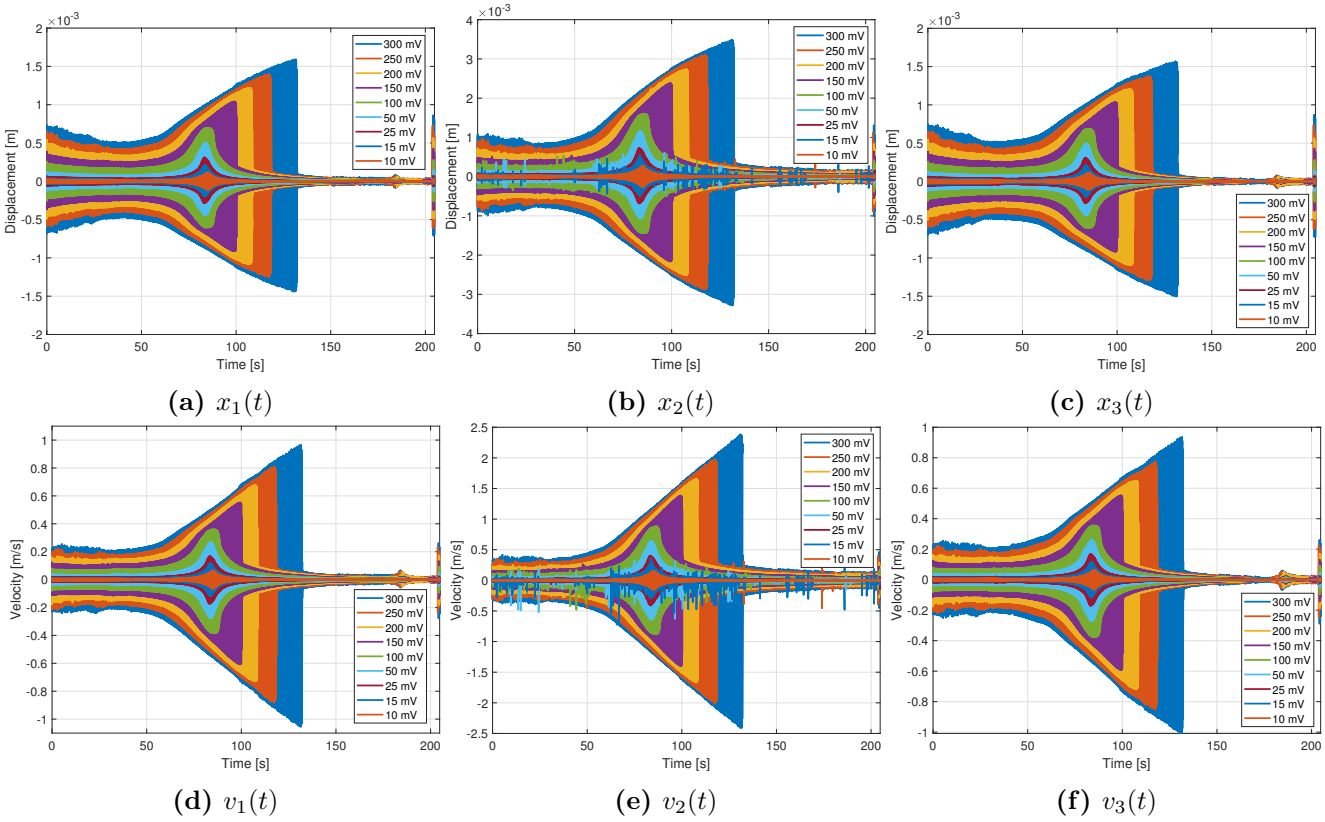

(a) $x_1(t)$ **(b)** $x_2(t)$ **(c)** $x_3(t)$

(d) $v_1(t)$ **(e)** $v_2(t)$ **(f)** $v_3(t)$

Fig. 12: Filtered **(a-c)** displacement and **(d-f)** velocity signals measured with the laser vibrometer and two accelerometers. Subscripts $k \in \{1, 2, 3\}$ of $x_k(t)$ and $v_k(t)$ correspond to those presented in Fig. 10a.

Tab. 13: Estimated values of the nonlinear coefficients obtained with the $\mathbf{D}_1$- and $\mathbf{D}_2$-based NIXO methods in Step 2 of the identification procedure. Rows in which the β_{111} satisfies the accuracy criteria (13) are marked with green. None of the other α_{uv} and β_{lmn} parameters satisfied these accuracy criteria. The units of β_{111} are $\frac{1}{\text{kg m}^2 \text{ s}^2}$.

NIXO D1

Case	Signal 1	Signal 2	β_{111} estimate	β_{111}^{real}	$Re\left\{\beta_{111}^{cmplx}\right\}$	$Im\left\{\beta_{111}^{cmplx}\right\}$	Δ_*	Δ_{**}
1	50	25	3.164e+13	3.077e+13	3.251e+13	-1.971e+13	5.36	39.37
2	100	50	2.317e+13	2.519e+13	2.115e+13	-3.986e+12	19.14	81.15
3	100	25	2.365e+13	2.444e+13	2.286e+13	-1.346e+13	6.89	41.11
4	150	100	1.958e+13	1.769e+13	2.148e+13	-4.201e+12	17.62	80.44
5	150	50	2.439e+13	2.290e+13	2.587e+13	-9.827e+12	11.50	62.02
6	150	25	2.399e+13	1.916e+13	2.883e+13	-1.029e+13	33.53	64.31
7	200	150	2.398e+13	2.396e+13	2.401e+13	-1.262e+12	0.22	94.74
8	200	100	2.311e+13	2.227e+13	2.396e+13	-1.832e+12	7.06	92.36
9	200	50	2.353e+13	2.406e+13	2.301e+13	-6.664e+12	4.54	71.04
10	200	25	2.345e+13	2.173e+13	2.516e+13	-1.257e+13	13.63	50.04
11	250	200	2.641e+13	2.632e+13	2.649e+13	1.461e+12	0.61	94.48
12	250	150	2.765e+13	2.772e+13	2.758e+13	3.936e+11	0.53	98.57
13	250	100	2.559e+13	2.545e+13	2.573e+13	-6.727e+11	1.10	97.39
14	250	50	2.474e+13	2.539e+13	2.410e+13	-4.264e+12	5.36	82.31
15	250	25	2.565e+13	2.382e+13	2.748e+13	-9.178e+12	13.30	66.60
16	300	250	3.245e+13	3.188e+13	3.303e+13	9.704e+11	3.50	97.06
17	300	200	3.168e+13	3.179e+13	3.157e+13	2.191e+12	0.72	93.06
18	300	150	3.131e+13	3.098e+13	3.165e+13	1.042e+12	2.11	96.71
19	300	100	2.864e+13	2.862e+13	2.865e+13	6.510e+11	0.11	97.73
20	300	50	2.683e+13	2.762e+13	2.604e+13	-3.446e+12	6.08	86.77
21	300	25	2.761e+13	2.838e+13	2.684e+13	-8.703e+12	5.76	67.57

NIXO D2

Case	Signal 1	Signal 2	β_{111} estimate	β_{111}^{real}	$Re\left\{\beta_{111}^{cmplx}\right\}$	$Im\left\{\beta_{111}^{cmplx}\right\}$	Δ_*	Δ_{**}
1	50	25	3.359e+13	3.972e+13	2.745e+13	-1.856e+13	44.70	32.39
2	100	50	2.053e+13	2.263e+13	1.842e+13	-5.121e+12	22.83	72.20
3	100	25	2.044e+13	2.040e+13	2.048e+13	-9.919e+12	0.37	51.56
4	150	100	1.733e+13	1.418e+13	2.047e+13	-2.337e+12	30.75	88.59
5	150	50	2.416e+13	2.709e+13	2.122e+13	-6.825e+12	27.63	67.84
6	150	25	2.227e+13	2.313e+13	2.141e+13	-1.097e+13	8.05	48.73
7	200	150	2.244e+13	2.303e+13	2.184e+13	-2.347e+12	5.46	89.25
8	200	100	2.129e+13	1.964e+13	2.294e+13	-1.290e+12	14.41	94.38
9	200	50	2.208e+13	2.373e+13	2.043e+13	-4.475e+12	16.13	78.09
10	200	25	2.198e+13	2.732e+13	1.665e+13	-7.664e+12	64.13	53.96
11	250	200	2.044e+13	2.094e+13	1.995e+13	2.158e+12	4.97	89.18
12	250	150	2.423e+13	2.475e+13	2.371e+13	-1.327e+12	4.36	94.40
13	250	100	2.343e+13	2.311e+13	2.374e+13	-1.815e+12	2.63	92.36
14	250	50	2.329e+13	2.525e+13	2.133e+13	-4.012e+12	18.39	81.19
15	250	25	2.510e+13	3.078e+13	1.942e+13	-5.597e+12	58.53	71.17
16	300	250	2.472e+13	2.569e+13	2.376e+13	-4.513e+11	8.13	98.10
17	300	200	2.344e+13	2.436e+13	2.252e+13	4.902e+11	8.16	97.82
18	300	150	2.435e+13	2.401e+13	2.468e+13	-2.319e+12	2.70	90.61
19	300	100	2.409e+13	2.371e+13	2.447e+13	-2.200e+12	3.13	91.01
20	300	50	2.301e+13	2.457e+13	2.144e+13	-5.043e+12	14.59	76.48
21	300	25	2.603e+13	3.239e+13	1.968e+13	-7.691e+12	64.63	60.91

5.4 Steps 2 and 3 of the System ID Procedure

The 21 signal pairs listed in Tab. 12 were provided to NIXO, and the algorithm returned the estimates of the linear and nonlinear parts of the model function in Eq. (22a). When it comes to the nonlinear part, the estimated values of seven polynomial coefficients were first computed, and then the Δ-metrics for each of the α and β parameters in each of the 21 cases run were found. The only parameter which consistently satisfied the criteria from Eq. (13) was β_{111} – and it only satisfied them in nine of the cases marked in green in Tab. 13. Interestingly, these correspond to cases where the first input signal was near its largest amplitude (200 to 300 mV) and the second signal was relatively large as well. These nine cases are summarized in Tab. 14. Even in these cases, the other nonlinear coefficients α_{11}, α_{12}, α_{22}, β_{112}, β_{122}, and β_{222} did not consistently satisfy the criteria from Eq. (13), and so they are not shown.

Tab. 14: The nine case studies that produced β_{111} terms satisfying the error metrics.

Voltage Amplitude $[mV]$		
1st Signal	2nd Signal	# of pairs
200	$\{150, 100\}$	2
250	$\{200, 150, 100\}$	3
300	$\{250, 200, 150, 100\}$	4
	Together:	9 pairs

Figure 13 presents the linear frequency response function returned by the NIXO procedure in this stage of the identification, i.e. when the nonlinear equation of motion was assumed to consist of seven polynomial terms. This frequency response function is the average of the nine FRF curves obtained in the cases specified in Tab. 14. The FRF curves found in each of these nine case studies can be viewed in Fig. 16 in Appendix A. Additionally, the average linear FRF is compared to the reference FRFs computed with the popular linear $\mathbf{H}_1$-estimator [46,47] applied to the low-amplitude

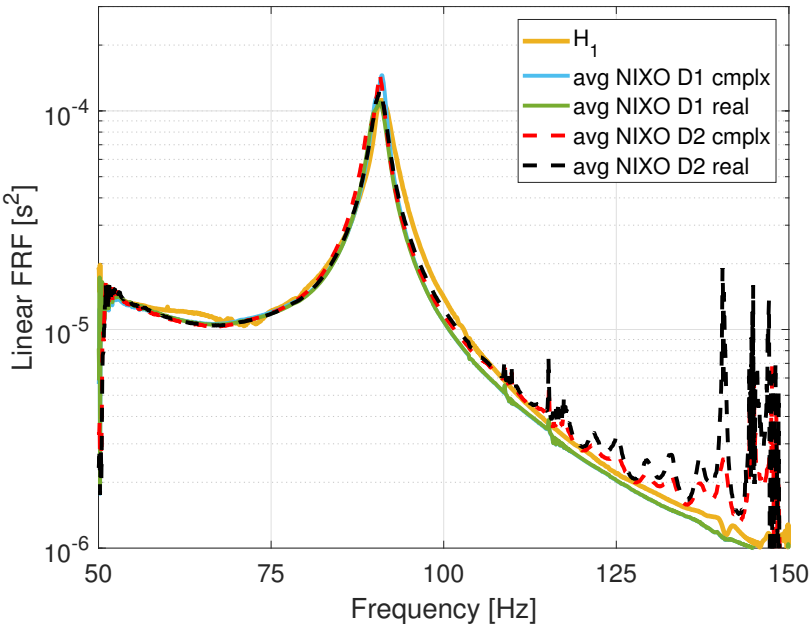

Fig. 13: Reference vs. average estimated linear FRFs. Step 2 of the identification procedure.

i/o signals. All four NIXO algorithms returned similar estimates for the FRF, although the results obtained with the $\mathbf{D}_2$-NIXO algorithm were much noisier away from the resonance.

Table 15 presents a quantitative comparison of the linear FRF estimates in Fig. 13; the natural frequency and damping were estimated from each FRF using AMI [45]. The relative differences between the linear natural frequencies is less than 1%, while the differences between the linear damping ratios are as large as 36%.

Tab. 15: Comparison of the modal parameters extracted from the average estimated and reference linear FRFs. Relative differences are calculated with respect to the results obtained with the linear $\mathbf{H}_1$-estimator applied to the low-amplitude i/o signals.

Algorithm	nat. freq [Hz]	rel. diff.	lin. damping	rel. diff.
H1	91.076		0.0119	
NIXO D1 cmplx	90.702	(0.41%)	0.0076	(36%)
NIXO D1 real	90.526	(0.60%)	0.0099	(16%)
NIXO D2 cmplx	90.274	(0.88%)	0.0084	(30%)
NIXO D2 real	90.651	(0.47%)	0.0110	(7.2%)

The proposed procedure found that out of the seven assumed nonlinear terms, only the cubic term β_{111} was identified as dominant. With only this term the equation of motion (22a) becomes Eq. (24).

$$\ddot{q}_1 + 2\zeta_1\omega_1\dot{q}_1 + \omega_1^2 q_1 + \beta_{111}^1 q_1^3 \quad = \mathbf{\Phi}_1^T \mathbf{f}(t) \tag{24}$$

To obtain a best estimate for β_{111} at this stage, the average was computed over all of the values in Table 13 whose Δ-metrics satisfy the accuracy criteria (i.e. the rows marked in green). The value of the β_{111} parameter thus obtained with $\mathbf{D}_1$-based NIXO is in the range $(2.31,\ 3.25)\times 10^{13}\frac{1}{\text{kg m}^2\ \text{s}^2}$, with an average value of $2.79\times 10^{13}\frac{1}{\text{kg m}^2\ \text{s}^2}$ and a relative standard deviation of 11.54 %. Results obtained with $\mathbf{D}_2$-based NIXO are: $\beta_{111} \in (2.04,\ 2.47)\times 10^{13}\frac{1}{\text{kg m}^2\ \text{s}^2}$ with an average of $2.32\times 10^{13}\frac{1}{\text{kg m}^2\ \text{s}^2}$ and relative standard deviation of 6.01%. However, the value obtained in this phase is not necessarily trustworthy and so the identification proceeds to the 4th step, where the identification is repeated with nonlinear EOM including only the β_{111} term.

5.5 Step 4 of the System ID Procedure

This section presents the outcomes from the identification attempt using the equation of motion in Eq. (24). Figure 14 and Table 16 show the results related to the linear part of the mechanical system. It is interesting to note that the average estimated linear FRFs is less accurate than that obtained previously. (Similarly to what was described in the Section 5.4 – the criteria from Eq. (13) were satisfied by the β_{111} coefficient only in the cases where the structure was oscillating at high enough amplitudes. These nine cases are marked in green in Tab. 17.) Quantifying the results in Table 16, this produces up to a 5% error in the natural frequency and up to 164% in the linear damping ratio. The FRF curves obtained in each of the above-mentioned nine individual cases are relegated to Appendix B.

Table 17 presents the estimates of the nonlinear β_{111} parameter for each of the 21 pairs of signals provided to NIXO. The rows in which the estimated β_{111} coefficients are strongly-real-valued are marked with green. From a statistical perspective, the value of the β_{111} parameter (obtained with $\mathbf{D}_1$-NIXO) ranges from 1.11×10^{13} to $1.86 \times 10^{13}\frac{1}{\text{kg m}^2\ \text{s}^2}$ with the average of $1.37 \times 10^{13}\frac{1}{\text{kg m}^2\ \text{s}^2}$

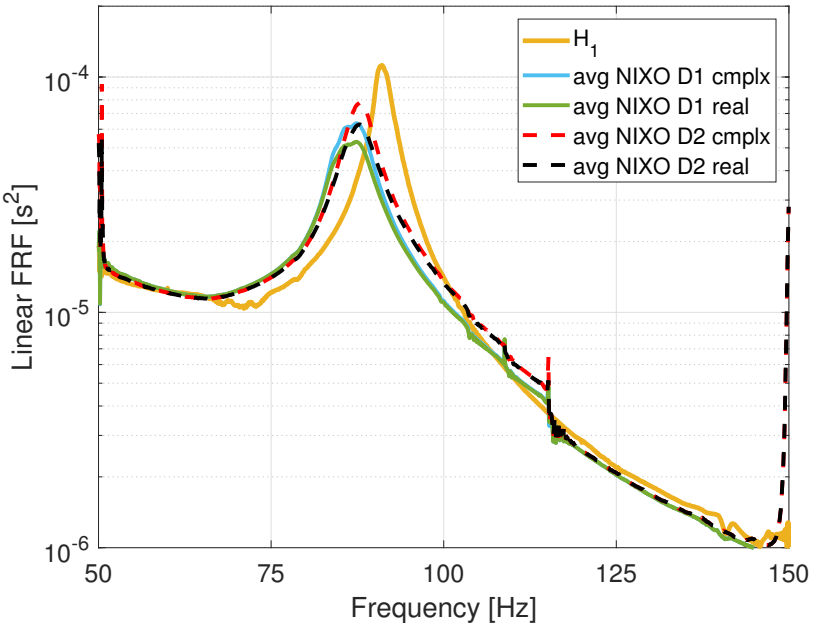

Fig. 14: Reference vs. average estimated linear FRFs. Step 4 of the identification procedure.

Tab. 16: Quantitative comparison of the average estimated and reference linear frequency response functions. Relative differences calculated with respect to the values obtained with the linear $\mathbf{H}_1$-estimator applied to the low-amplitude i/o signals.

Algorithm	nat. freq [Hz]	rel. diff.	lin. damping	rel. diff.
H1	91.076		0.0119	
NIXO D1 cmplx	86.686	(4.82%)	0.0273	(129.94%)
NIXO D1 real	86.492	(5.03%)	0.0314	(164.52%)
NIXO D2 cmplx	87.763	(3.64%)	0.0230	(94.07%)
NIXO D2 real	87.593	(3.82%)	0.0279	(135.51%)

and relative standard deviation of 17.69%. The $\mathbf{D}_2$-based algorithm produced fairly similar results, giving $\beta_{111} \in (1.01, 1.32) \times 10^{13} \frac{1}{\text{kg m}^2 \text{ s}^2}$ with the average and the relative standard deviation of, respectively, $1.13 \times 10^{13} \frac{1}{\text{kg m}^2 \text{ s}^2}$ and 8.28%.

In order to evaluate the nonlinear parameter values returned by NIXO, the NNMs of the system in Eq. (24) were computed for the identified range of β_{111}. They are overlaid on the displacement and velocity time signals in Fig. 15. Additionally, the nonlinear normal modes computed for the average β_{111} values from Steps 2 and 3 of the proposed procedure (i.e. $\beta_{111} = 2.79 \times 10^{13} \frac{1}{\text{kg m}^2 \text{ s}^2}$ and $\beta_{111} = 2.32 \times 10^{13} \frac{1}{\text{kg m}^2 \text{ s}^2}$) are also shown. The NNMs obtained using the values of β_{111} from Steps 2 and 3 clearly do not agree with the signals, but the range of β_{111} values identified in Step 4 does seem to be more accurate. However, even these values of β_{111} do not capture the peaks of the swept-sines for 25-100 mV, so perhaps the the model would be more accurate if an additional nonlinear term, not identified by the NIXO algorithms, was added to equation of motion (24). This also might explain why the linear FRFs obtained in Steps 2 and 3 appeared to be more accurate for this particular structure.

Tab. 17: Estimated values of the β_{111} coefficient obtained with $\mathbf{D}_1$- and $\mathbf{D}_2$-based NIXO in Step 4 of the identification procedure. The rows where the β_{111} coefficient satisfies the accuracy criteria (13) are marked with green. The units of β_{111} are $\frac{1}{\text{kg m}^2 \text{ s}^2}$.

NIXO D1

Case	Signal 1	Signal 2	β_{111} estimate	β_{111}^{real}	$Re\left\{\beta_{111}^{cmplx}\right\}$	$Im\left\{\beta_{111}^{cmplx}\right\}$	Δ_*	Δ_{**}
1	50	25	-1.144e+12	-1.144e+12	-1.144e+12	4.351e+12	0.00	280.23
2	100	50	4.784e+12	4.784e+12	4.784e+12	3.482e+12	0.00	27.20
3	100	25	2.996e+12	2.996e+12	2.996e+12	3.724e+12	0.00	24.28
4	150	100	1.107e+13	1.107e+13	1.107e+13	1.184e+12	0.00	89.30
5	150	50	8.032e+12	8.032e+12	8.032e+12	2.229e+12	0.00	72.25
6	150	25	6.257e+12	6.257e+12	6.257e+12	2.643e+12	0.00	57.76
7	200	150	1.320e+13	1.320e+13	1.320e+13	1.028e+12	0.00	92.21
8	200	100	1.125e+13	1.125e+13	1.125e+13	1.143e+12	0.00	89.84
9	200	50	8.832e+12	8.832e+12	8.832e+12	1.828e+12	0.00	79.30
10	200	25	7.297e+12	7.297e+12	7.297e+12	2.135e+12	0.00	70.74
11	250	200	1.620e+13	1.620e+13	1.620e+13	1.426e+12	0.00	91.20
12	250	150	1.315e+13	1.315e+13	1.315e+13	1.377e+12	0.00	89.53
13	250	100	1.125e+13	1.125e+13	1.125e+13	1.392e+12	0.00	87.63
14	250	50	8.941e+12	8.941e+12	8.941e+12	1.897e+12	0.00	78.79
15	250	25	7.575e+12	7.575e+12	7.575e+12	2.110e+12	0.00	72.14
16	300	250	1.860e+13	1.860e+13	1.860e+13	1.173e+12	0.00	93.70
17	300	200	1.564e+13	1.564e+13	1.564e+13	1.348e+12	0.00	91.38
18	300	150	1.309e+13	1.309e+13	1.309e+13	1.293e+12	0.00	90.13
19	300	100	1.140e+13	1.140e+13	1.140e+13	1.364e+12	0.00	88.03
20	300	50	9.266e+12	9.266e+12	9.266e+12	1.775e+12	0.00	80.85
21	300	25	7.992e+12	7.992e+12	7.992e+12	1.968e+12	0.00	75.38

NIXO D2

Case	Signal 1	Signal 2	β_{111} estimate	β_{111}^{real}	$Re\left\{\beta_{111}^{cmplx}\right\}$	$Im\left\{\beta_{111}^{cmplx}\right\}$	Δ_*	Δ_{**}
1	50	25	-4.624e+11	-4.624e+11	-4.624e+11	3.828e+12	0.00	727.87
2	100	50	5.306e+12	5.306e+12	5.306e+12	3.300e+12	0.00	37.81
3	100	25	3.436e+12	3.436e+12	3.436e+12	3.453e+12	0.00	0.49
4	150	100	1.093e+13	1.093e+13	1.093e+13	1.104e+12	0.00	89.90
5	150	50	7.635e+12	7.635e+12	7.635e+12	2.651e+12	0.00	65.29
6	150	25	5.826e+12	5.826e+12	5.826e+12	2.976e+12	0.00	48.93
7	200	150	1.112e+13	1.112e+13	1.112e+13	6.032e+11	0.00	94.58
8	200	100	1.043e+13	1.043e+13	1.043e+13	9.600e+11	0.00	90.80
9	200	50	8.082e+12	8.082e+12	8.082e+12	2.152e+12	0.00	73.38
10	200	25	6.605e+12	6.605e+12	6.605e+12	2.437e+12	0.00	63.10
11	250	200	1.236e+13	1.236e+13	1.236e+13	1.588e+12	0.00	87.15
12	250	150	1.093e+13	1.093e+13	1.093e+13	1.324e+12	0.00	87.88
13	250	100	1.011e+13	1.011e+13	1.011e+13	1.310e+12	0.00	87.04
14	250	50	8.242e+12	8.242e+12	8.242e+12	2.162e+12	0.00	73.77
15	250	25	6.970e+12	6.970e+12	6.970e+12	2.374e+12	0.00	65.95
16	300	250	1.322e+13	1.322e+13	1.322e+13	6.080e+11	0.00	95.40
17	300	200	1.201e+13	1.201e+13	1.201e+13	1.104e+12	0.00	90.81
18	300	150	1.094e+13	1.094e+13	1.094e+13	1.111e+12	0.00	89.85
19	300	100	1.010e+13	1.010e+13	1.010e+13	1.279e+12	0.00	87.35
20	300	50	8.491e+12	8.491e+12	8.491e+12	2.006e+12	0.00	76.37
21	300	25	7.326e+12	7.326e+12	7.326e+12	2.210e+12	0.00	69.84

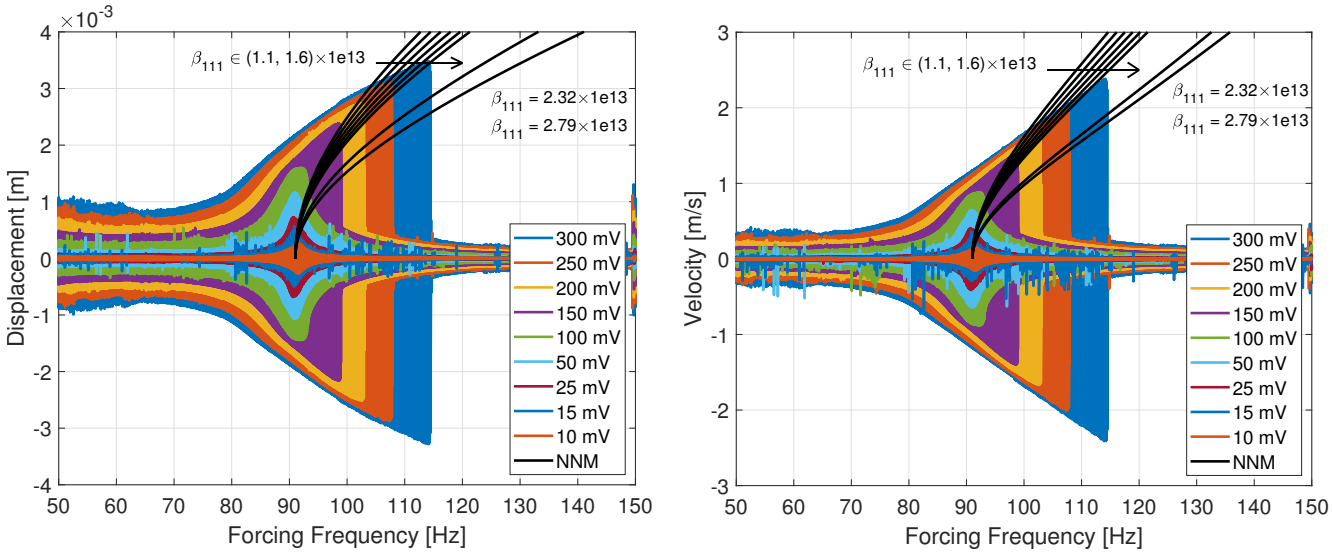

(a) **(b)**

Fig. 15: The NNM curves computed for the identified EOM overlayed on the **(a)** displacement and **(b)** velocity time signals.

6 Conclusion and Future Work

This work has presented a novel black-box system identification technique, which is based on the NIXO algorithm, and its application to geometrically nonlinear structures. The procedure begins with postulating a general form of the nonlinear equation of motion. Then NIXO is applied to the input and output signals collected experimentally, and two metrics that are inherent to NIXO are used to identify and eliminate the unimportant nonlinear terms from the postulated governing equation. The process ends with repeating the identification, however, this time utilizing the reduced nonlinear EOM.

The proposed black-box technique was evaluated by applying it to two case studies, one numerical and the other one experimental. In the numerical case study, the algorithm needed only the first three steps, in which it identified which four polynomial terms (out of initially assumed 16 terms) should be considered dominant in the mechanical system. Additionally, the algorithm simultaneously found accurate values for the polynomial coefficients. In Step 4, the method revealed that two of these terms were most likely more important than the other two. However, trial and error disclosed that all four polynomial terms should be kept in order to accurately estimate the NNM of the numerical system.

As one might expect, it was more challenging to apply the algorithm to actual experimental measurements, which are subject to noise and other contamination. Namely, the three-step procedure found a relatively accurate estimate of the underlying linear system and pointed out which nonlinear term was dominant in the equation of motion. However, if the algorithm was terminated at that point then the values obtained for the nonlinear parameter seemed to be significantly in error. In the fourth step, NIXO returned more accurate values of the nonlinear coefficient, but the linear system was approximated with less accuracy. It seems reasonable to speculate that reducing the size of the postulated EOM improves the numerical conditioning of the nonlinear identification

problem, allowing the nonlinear parameter to be identified more accurately. However, with the other nonlinear terms absent, the nonlinear model proves somewhat inadequate to describe all that is present in the measurements, and so the estimate of the linear FRF becomes less accurate.

The observations above may indicate that the nonlinear model might be considered not complete. The general form used was based on the assumption that geometric nonlinearity was the dominant effect. However, nonlinear damping and cross-terms such as $c_1\dot{q}_1^2 + c_2\dot{q}_1 q_1^2 + ...$ may be missing from Eq. (22a), which is the general EOM postulated. These missing terms could account for the impact of the environment on the oscillating beam, such as aerodynamic drag. Recent studies suggest that including such terms in the EOM is important, even for structures designed to be predominantly geometrically nonlinear [48]. Hence, even though the model form considered here is suitable to capture a very wide range of geometrically nonlinear behavior, including softening and hardening effects, it may not be general enough.

Future work will investigate potential differences between the simulated and experimental studies presented in this paper. One possible approach would be to introduce simulated noise into the numerical output signals to determine whether this explains the discrepancies. However, it should be noted that the noise present in real measurements is often not simply Gaussian. Additionally, a case study should also be conducted examining the impact of potentially missing nonlinear damping and cross terms, such as $c_1\dot{q}_1^2 + c_2\dot{q}_1 q_1^2 + ...$, on the identification results. Finally, to explore the limitations of the NIXO-based technique, it would be interesting to apply it to mechanical systems with non-geometric nonlinearities, such as frictional nonlinearity, or to systems with two nonlinear normal modes that have close natural frequencies and may interact with each other.

Appendices

A Individual Linear FRF Results from Steps 2 and 3 of the Experimental Case Study

Figure 16 presents the linear frequency response functions found in the nine case studies marked with green in Tab. 13. In these system identification attempts only, the Δ-metrics satisfy the criteria from Eq. (13). Additionally, the FRF curves are compared to the reference ones obtained with the linear $\mathbf{H}_1$-estimator applied to the low-amplitude i/o signals. The results from these nine subplots shown were averaged to obtain the linear FRF estimate shown in Fig. 13.

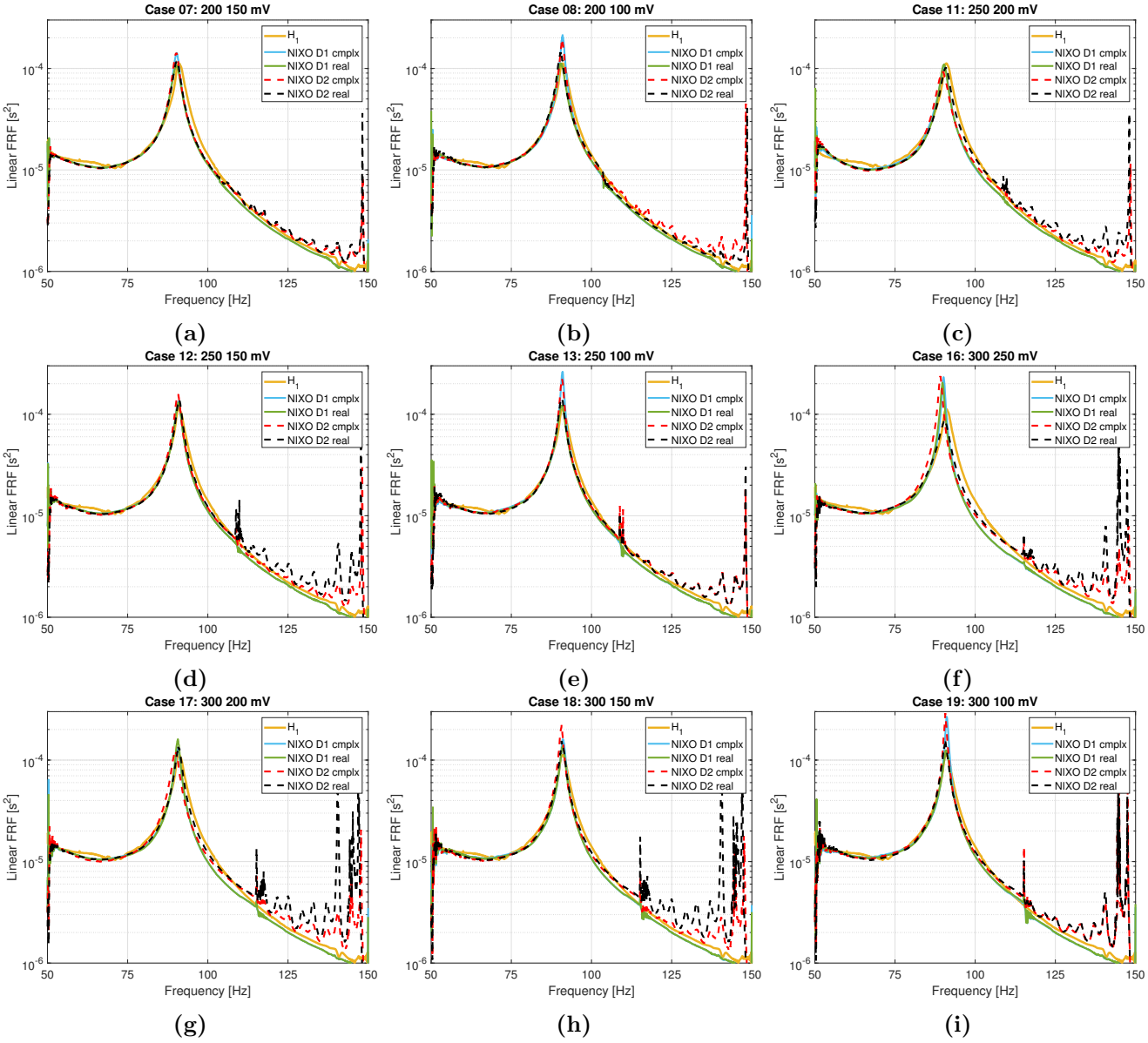

Fig. 16: Linear FRFs pertaining to the identification attempts marked with green in Tab. 13.

B Individual Linear FRF Results from Step 4 of the Experimental Case Study

Figure 17 presents the linear frequency response functions found in the nine case studies marked with green in Tab. 17. In these system identification attempts only, the Δ-metrics satisfy the criteria introduced from Eq. (13). Additionally, the FRF curves are compared to the reference ones obtained with the linear $\mathbf{H}_1$-estimators applied to the low-amplitude i/o signals. The results from these nine subplots were averaged to obtain the linear FRF estimate shown in Fig. 14.

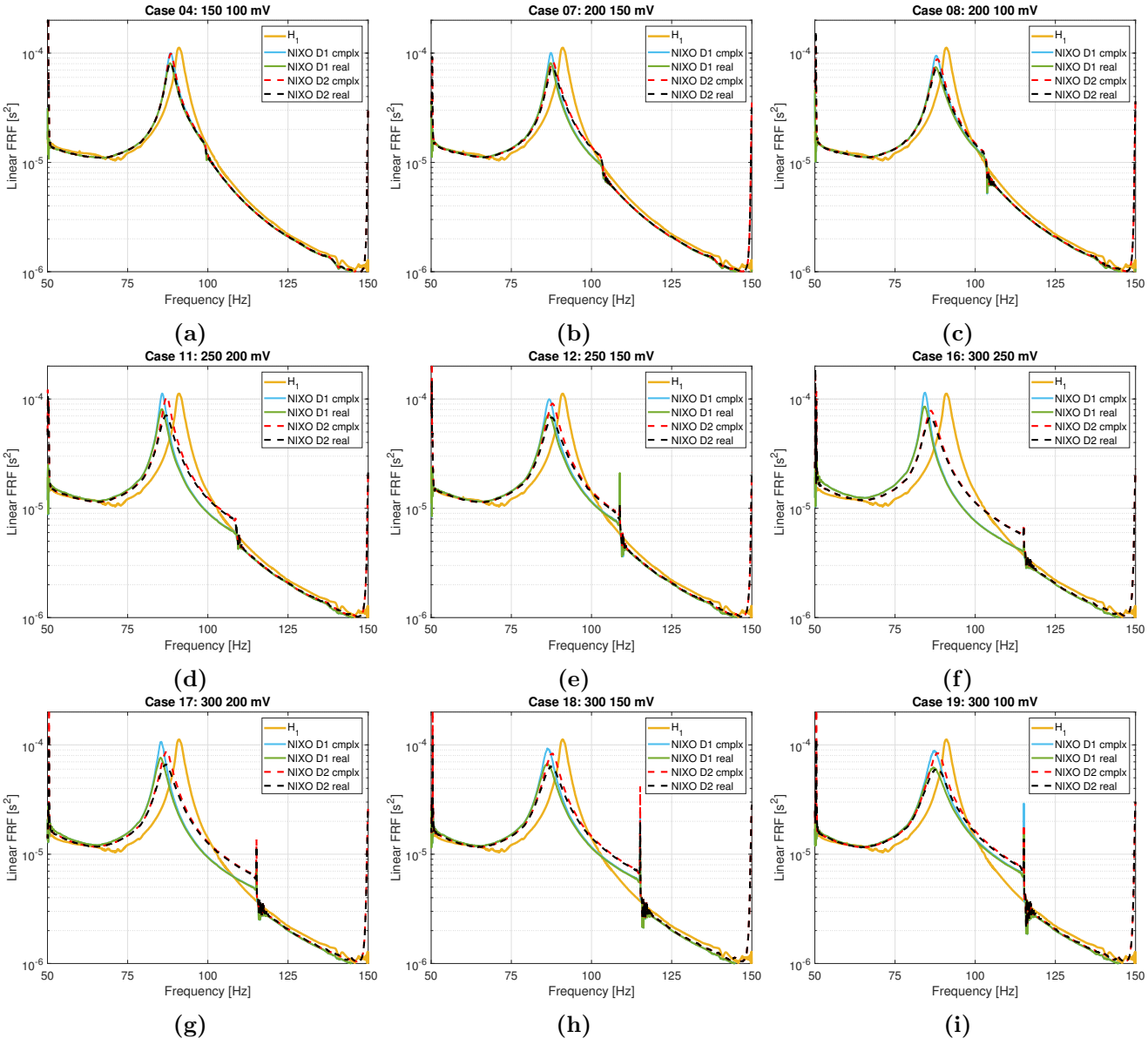

Fig. 17: Linear FRFs pertaining to the identification attempts marked with green in Tab. 17.

References

[1] Porter, J. H., Balaji, N. N., and Brake, M. R. W., 2022. "A Non-Masing Microslip Rough Contact Modeling Framework for Spatially and Cyclically Varying Normal Pressure". In Nonlinear Structures & Systems, Volume 1, G. Kerschen, M. R. Brake, and L. Renson, eds., Springer International Publishing, pp. 53–59.

[2] Estakhraji, S. I. Z., and Allen, M. S., 2022. "Extension of the Harmonic Balance Method for dynamic systems with Iwan joints". *Mechanical Systems and Signal Processing,* **166**, p. 108434.

[3] Hollkamp, J. J., Gordon, R. W., and Spottswood, S. M., 2005. "Nonlinear modal models for sonic fatigue response prediction: a comparison of methods". *Journal of Sound and Vibration,* **284**(3), pp. 1145 – 1163.

[4] Mignolet, M. P., Przekop, A., Rizzi, S. A., and Spottswood, S. M., 2013. "A review of indirect/non-intrusive reduced order modeling of nonlinear geometric structures". *Journal of Sound and Vibration,* **332**(10), pp. 2437–2460. Number: 10.

[5] Karamooz Mahdiabadi, M., Tiso, P., Brandt, A., and Rixen, D. J., 2021. "A non-intrusive model-order reduction of geometrically nonlinear structural dynamics using modal derivatives". *Mechanical Systems and Signal Processing,* **147**, p. 107126.

[6] Brown, J. D., Wang, C., and Moore, K. J., 2022. "Multi-dimensional Vibration Mitigation Using a Nonlinear Vibration Absorber with Impact and Sliding Along an Elliptical Frame". In Proceedings of the 40th International Modal Analysis Conference (IMAC), Orlando FL, USA.

[7] Wang, C., Allen, A. T., Krings, E. J., Markvicka, E. J., and Moore, K. J., 2022. "Applying Quasi-zero Stiffness Introduced by Elastic Strut Elements to Achieve Energy Isolation and Dissipation". In Proceedings of the 40th International Modal Analysis Conference (IMAC), Orlando FL, USA.

[8] Theurich, T., and Krack, M., 2023. "Experimental validation of impact energy scattering as concept for mitigating resonant vibrations.". *Journal of Structural Dynamics,* **2**, pp. 1–23.

[9] Chen, C., and Duffour, P., 2018. "Modelling Damping Sources in Monopile-supported Offshore Wind Turbines". *Wind Energy,* **21**, 06.

[10] Ginsberg, J. H., 2001. *Mechanical and Structural Vibrations: Theory and Applications*. New York: Wiley, First edition.

[11] Kerschen, G., Peeters, M., Golinval, J., and Vakakis, A., 2009. "Nonlinear normal modes, Part I: A useful framework for the structural dynamicist". *Mechanical Systems and Signal Processing,* **23**(1), pp. 170 – 194. Special Issue: Non-linear Structural Dynamics.

[12] Vakakis, A. F., McFarland, D. M., Bergman, L., Manevitch, L. I., and Gendelman, O., 2004. "Isolated Resonance Captures and Resonance Capture Cascades Leading to Single- or Multi-Mode Passive Energy Pumping in Damped Coupled Oscillators". *Journal of Vibration and Acoustics,* **126**(2), 05, pp. 235–244.

[13] Nayfeh, A., and Mook, D., 2008. *Nonlinear Oscillations*. Wiley Classics Library. Wiley.

[14] Vakakis, A. F., Manevitch, L. I., Mikhlin, Y. v., Pilipchuk, V. N., , and A, Z. A., 1996. *Normal Modes and Localization in Nonlinear Systems*. Wiley.

[15] Kerschen, G., Worden, K., Vakakis, A. F., and Golinval, J.-C., 2006. "Past, present and future of nonlinear system identification in structural dynamics". *Mechanical Systems and Signal Processing,* **20**(3), pp. 505 – 592.

[16] Bonisoli, E., and Vigliani, A., 2007. "Identification techniques applied to a passive elasto-magnetic suspension". *Mechanical Systems and Signal Processing,* **21**(3), pp. 1479 – 1488.

[17] Göge, D., and Sinapius, J. M., 2006. "Experiences with dynamic load simulation by means of modal forces in the presence of structural non-linearities". *Aerospace Science and Technology,* **10**(5), pp. 411 – 419.

[18] Adams, D., and Allemang, R., 2000. "A Frequency Domain Method for Estimating the Parameters of a Non-Linear Structural Dynamic Model Through Feedback". *Mechanical Systems and Signal Processing,* **14**(4), pp. 637 – 656.

[19] Haroon, M., and Adams, D. E., 2009. "A modified H_2 algorithm for improved frequency response function and nonlinear parameter estimation". *Journal of Sound and Vibration,* **320**, 03, pp. 822–837.

[20] Spottswood, S., and Allemang, R., 2006. "Identification of nonlinear parameters for reduced order models". *Journal of Sound and Vibration,* **295**(1), pp. 226 – 245.

[21] Kwarta, M., and Allen, M. S., 2021. "Extensions to NIFO and CRP to Estimate Frequency-Independent Nonlinear Parameters". In Special Topics in Structural Dynamics & Experimental Techniques, Volume 5, D. S. Epp, ed., Springer International Publishing, pp. 99–119.

[22] Kwarta, M., and Allen, M. S., 2023. "Nonlinear Identification through eXtended Outputs (NIXO) with numerical and experimental validation using geometrically nonlinear structures". *Mechanical Systems and Signal Processing,* **200**, p. 110542.

[23] Feldman, M., 2011. *Hilbert Transform Applications in Mechanical Vibration*. John Wiley and Sons.

[24] Carrella, A., and Ewins, D., 2011. "Identifying and quantifying structural nonlinearities in engineering applications from measured frequency response functions". *Mechanical Systems and Signal Processing,* **25**(3), pp. 1011 – 1027.

[25] Karaağaçlı, T., and Özgüven, H. N., 2021. "Experimental modal analysis of nonlinear systems by using response-controlled stepped-sine testing". *Mechanical Systems and Signal Processing,* **146**, p. 107023.

[26] Kwarta, M., and Allen, M. S., 2022. "Nonlinear Normal Mode backbone estimation with near-resonant steady state inputs". *Mechanical Systems and Signal Processing,* **162**, p. 108046.

[27] Szemplińska-Stupnicka, W., 1979. "The modified single mode method in the investigations of the resonant vibrations of non-linear systems". *Journal of Sound and Vibration,* **63**(4), pp. 475 – 489.

[28] Chen, Q., Worden, K., Peng, P., and Leung, A., 2007. "Genetic algorithm with an improved fitness function for (N)ARX modelling". *Mechanical Systems and Signal Processing,* **21**(2), pp. 994 – 1007.

[29] Worden, K., Wong, C., Parlitz, U., Hornstein, A., Engster, D., Tjahjowidodo, T., Al-Bender, F., Rizos, D., and Fassois, S., 2007. "Identification of pre-sliding and sliding friction dynamics: Grey box and black-box models". *Mechanical Systems and Signal Processing,* **21**(1), pp. 514–534.

[30] Moore, K. J., 2019. "Characteristic nonlinear system identification: A data-driven approach for local nonlinear attachments". *Mechanical Systems and Signal Processing,* **131**, pp. 335–347.

[31] Singh, A., and Moore, K. J., 2022. "Data-Driven Identification of Multiple Local Nonlinear Attachments Installed on a Single Primary Structure". In Proceedings of the 40th International Modal Analysis Conference (IMAC), Orlando, FL, USA.

[32] Li, S., and Yang, Y., 2022. "Data-driven Nonlinear Modal Analysis: A Deep Learning Approach". In Proceedings of the 40th International Modal Analysis Conference (IMAC), Orlando, FL, USA.

[33] Duffing, G., 1918. *Erzwungene schwingungen bei veränderlicher eigenfrequenz und ihre technische bedeutung (Forced Oscillations in the Presence of Variable Eigenfrequencies and Their Technical Significance).* Braunschweig: F. Vieweg und sohn.

[34] Noël, J., Kerschen, G., Foltête, E., and Cogan, S., 2014. "Grey-box identification of a non-linear solar array structure using cubic splines". *International Journal of Non-Linear Mechanics,* **67**, pp. 106–119.

[35] Zhang, S., and Cross, E. J., 2022. "Grey-Box Modelling via Gaussian Process Mean Functions for Mechanical Systems". In Data Science in Engineering, Volume 9, R. Madarshahian and F. Hemez, eds., Springer International Publishing, pp. 161–168.

[36] Kwarta, M., and Allen, M. S., 2022. "NIXO-Based Identification of the Dominant Terms in a Nonlinear Equation of Motion". In Nonlinear Structures & Systems, Volume 1, G. Kerschen, M. R. Brake, and L. Renson, eds., Springer International Publishing, pp. 113–117.

[37] Kwarta, M., and Allen, M. S., 2023. "Application of Black-Box NIXO to Experimental Measurements". In Nonlinear Structures & Systems, Volume 1, M. R. Brake, L. Renson, R. J. Kuether, and P. Tiso, eds., Springer International Publishing, pp. 237–240.

[38] Platten, M., Wright, J., Dimitriadis, G., and Cooper, J., 2009. "Identification of multi-degree of freedom non-linear systems using an extended modal space model". *Mechanical Systems and Signal Processing,* **23**(1), pp. 8–29. Special Issue: Non-linear Structural Dynamics.

[39] Anastasio, D., Marchesiello, S., Kerschen, G., and Noël, J., 2019. "Experimental identification of distributed nonlinearities in the modal domain". *Journal of Sound and Vibration,* **458**, pp. 426–444.

[40] Van Damme, C., Allen, M., and Hollkamp, J., 2020. "Evaluating reduced order models of curved beams for random response prediction using static equilibrium paths". *Journal of Sound and Vibration,* **468**, p. 115018.

[41] Detroux, T., Renson, L., and Kerschen, G., 2014. "The harmonic balance method for advanced analysis and design of nonlinear mechanical systems". In Nonlinear Dynamics, Volume 2, G. Kerschen, ed., Springer International Publishing, pp. 19–34.

[42] Detroux, T., Renson, L., Masset, L., and Kerschen, G., 2015. "The harmonic balance method for bifurcation analysis of large-scale nonlinear mechanical systems". *Computer Methods in Applied Mechanics and Engineering,* **296**, pp. 18 – 38.

[43] Krack, M., and Gross, J., 2019. *Harmonic Balance for Nonlinear Vibration Problems*. Springer International Publishing, 03.

[44] Bendat, J. S., and Piersol, A. G., 1980. *Engineering Applications of Correlation and Spectral Analysis*. Wiley, New York.

[45] Allen, M. S., and Ginsberg, J. H., 2006. "A global, single-input–multi-output (SIMO) implementation of the algorithm of mode isolation and application to analytical and experimental data". *Mechanical Systems and Signal Processing,* **20**(5).

[46] H. Vold, J. Crowley, G. R., 1985. "A Comparison of H_1, H_2 and H_v Frequency Response Functions". In Proceedings of the International Modal Analysis Conference, pp. 272–278.

[47] Napolitano, K. L., 2016. "Using singular value decomposition to estimate frequency response functions". In Topics in Modal Analysis & Testing, Volume 10, M. Mains, ed., Springer International Publishing, pp. 27–43.

[48] Breunung, T., Cilenti, L., You, J. M., and Balachandran, B., 2023. "Robust Identification of Nonlinear Oscillators fromFrequency Response Data". In Proceedings of the 41th International Modal Analysis Conference (IMAC), Austin TX, USA.